Transport structure of the South Atlantic Ocean derived from a high-resolution numerical model and observations

Xiaobiao Xu*

COAPS/Florida State University, Tallahassee, Florida

Eric P. Chassignet

COAPS/Florida State University, Tallahassee, Florida

Shenfu Dong

AOML/National Oceanic and Atmospheric Administration, Miami, Florida

Molly O. Baringer

AOML/National Oceanic and Atmospheric Administration, Miami, Florida

Corresponding author: Xiaobiao Xu (xxu3@fsu.edu)

2000 Levy Avenue, Building A, Tallahassee FL 30306

Key Points:

1. The upper limb of the AMOC originates from the warm Indian Ocean water through the Agulhas Leakage
2. The NADW in the lower limb of AMOC flows southward as a DWBC to 45S and then turns eastward to flow across the Mid-Atlantic Ridge near 42S
3. The AMOC variability at seasonal to decadal timescales is latitudinally coherent from 35S to about 35N

Abstract

The South Atlantic Ocean plays an important role in the Atlantic meridional overturning circulation (AMOC), connecting it to the Indian and Pacific Oceans as part of the global overturning circulation system; yet, the detailed time mean circulation structure in this region and the large-scale spatial pattern of the AMOC variability remain unclear. Using model outputs from a 50-year, eddying global ocean-sea ice simulation validated against observations at a zonal section at 34°S, a meridional section at 65°W in the Drake Passage, and a meridional section southwest of Africa, we find that the upper limb of the AMOC originates from the Agulhas leakage and that while the cold Pacific water from the Drake Passage does not contribute directly to the AMOC it does play a significant role in setting the temperature and salinity properties of the water in the subtropical South Atlantic. We also find that the North Atlantic deep water (NADW) in the lower limb of AMOC flows southward as a deep western boundary current all the way to 45°S and then turns eastward to flow across the Mid-Atlantic Ridge near 42°S, and that the recirculation around the Vitoria-Trindade seamount chain brings some NADW into the Brazil Basin interior. Finally, we find that the AMOC variability is coherent on seasonal to decadal timescales from 35°S to about 35°N, where diapycnal water mass transformations between the upper and lower limbs of the AMOC are expected to be small.

1. Introduction

In the Atlantic Ocean, warm water from the South Atlantic flows northward in approximately the upper 1000 meters, loses buoyancy to the atmosphere by cooling *en route* to the northern North Atlantic, and eventually sinks and returns southward at depth as the cold North Atlantic Deep Water (NADW). The temperature difference between the upper and lower limbs of this Atlantic meridional overturning circulation (AMOC) leads to a large northward oceanic heat transport throughout the entire Atlantic basin, in contrast to the poleward heat transport in the Indo-Pacific Ocean (e.g., Macdonald and Baringer, 2013). The South Atlantic Ocean, defined here as the area south of 20°S (Figure 1), plays an important role in that it is through this region where the upper and lower AMOC limbs are connected to the Indian and Pacific Oceans and are entangled in the global overturning circulation system (e.g., Gordon, 1986; Broecker, 1991; Schmitz, 1995, 1996; Richardson 2008; Talley, 2013). Thus, a comprehensive knowledge of the circulation in this region is essential to our understanding of the spatial structure and temporal variability of the AMOC.

Significant observations have been made in the last 10 years or so toward quantifying and monitoring the AMOC in the South Atlantic, particularly along a latitude near 34.5°S (e.g., Baringer and Garzoli, 2007; Dong et al., 2009, 2014, 2015; Garzoli et al., 2013; Goes et al., 2015; Meinen et al., 2013; 2018). These observations, which consist of moorings, expendable Bathythermograph (XBT), and Argo float measurements, yield a time mean AMOC transport on the order of 14-20 Sv. They also show that there is significant AMOC variability on several timescales, similar to that observed by the RAPID array at 26.5°N (e.g., McCathy et al., 2015). Beyond 34.5°S, however, the observations in the South Atlantic remain sparse and short (in time). Overall, our understanding of the spatial structure of the time mean circulation is mostly limited to the schematic of Stramma and England (1999) and even less is known about its temporal variability.

In particular, there is a long-standing debate regarding the source of the upper limb of the AMOC (Gordon, 2001); whether it originates from the warm, saline Indian waters through the southern rim of Africa (e.g., Gordon 1986; Saunders and King 1995) or from the cooler, fresher Pacific water through the Drake Passage (e.g., Rintoul, 1991; Schlitzer, 1996). Although recent studies seem to favor the warm water route from the Indian Ocean through the Agulhas leakage (e.g., Richardson 2007; Beal et al., 2011), the relative contributions of cold versus warm water is still uncertain (Garzoli and Matano, 2011). At depth, in the lower limb of the AMOC, much attention has been paid to an eastward flow of the NADW near 22°S (e.g., Speer et al., 1995; Stramma and England, 1999; Arhan et al., 2003; Hogg and Thurnherr, 2005; Garzoli et al., 2015). This eastward transport is relatively minor when compared to the main branch of NADW, which continues to flow southward as the deep western boundary current (DWBC) along the deep continental slope of South America. However, the exact location of where the DWBC turns eastward south of 34°S and flows across the Mid-Atlantic Ridge (MAR) is largely unknown. Finally, there is also the underlying question as to whether the AMOC variability is meridionally coherent throughout the whole Atlantic (Kelly et al., 2004; Xu et al., 2014).

Three-dimensional circulation information beyond the existing observations is required in order to address the above questions. In this paper, we use a high-resolution numerical model to investigate the structure of the mean circulation in the South Atlantic as well as the temporal variability of the AMOC on basin scales. The paper is structured as follows: Section

2 summarizes the basic features of the numerical simulation. Section 3 examines the modeled large-scale circulation pattern and the circulation structure at three key observation locations: 34°S across the South Atlantic, 65°W in the Drake Passage, and along a Prime Meridian-Good Hope section southwest of Africa (Figure 1). The model results are shown to be in good agreement with the observed transports and are then used to document the time mean circulation pattern in the South Atlantic (Section 4) and the latitudinal coherence of the AMOC variability throughout the Atlantic basin (Section 5). Summary and discussions follow in Section 6.

2. Numerical Simulation

The numerical results presented in this study are from a long-term global ocean-sea ice hindcast simulation performed using the Hybrid Coordinate Ocean Model (HYCOM, Bleck, 2002; Chassignet et al., 2003), coupled with the Community Ice CodE (CICE, Hunke and Lipscomb, 2008). The vertical coordinate of the HYCOM is isopycnic in the stratified open ocean and makes a dynamically smooth and time-dependent transition to terrain following in the shallow coastal regions and to fixed pressure levels in the surface mixed layer and/or unstratified seas. In doing so, the model combines the advantages of the different coordinate types in simulating coastal and open ocean circulation features simultaneously (e.g., Chassignet et al., 2006).

The simulation has a horizontal resolution of 1/12° (~6 km in the area of interest) and a vertical resolution of 36 layers (in σ_2). It is initialized using the January temperature and salinity from an ocean climatology (Carnes, 2009) and is forced using the 3-hourly, 0.7° DRAKKAR forcing set DFS5.2 (Dussin et al., 2016). The DFS5.2 combines two ECMWF

(European Centre for Medium-range Weather Forecast) reanalysis products, ERA40 and ERA-interim, and covers the time period of 1958-2015. The surface heat flux forcing is computed using the shortwave and longwave radiations from DFS5.2, as well as the latent and sensible heat fluxes derived from the CORE bulk formulae of Large and Yeager (2004) and the model sea surface temperature (SST). The surface freshwater forcing includes evaporation, precipitation, and climatological river runoffs. In addition, the model sea surface salinity (SSS) is restored toward ocean climatology with a restoring timescale of two months and it is constrained by an ad hoc assumption of zero global net flux at each time step. The wind stress is calculated from the atmospheric wind velocity and does not take into account the shear introduced by the ocean currents. The simulation starts from rest and is integrated over 1958-2015 with no data assimilation. The horizontal diffusion parameters are listed in Table 1. In this study, we focus on the last 35 years of the simulation (1981-2015) as being representative of the time-mean circulation after spin-up (see Figure 2 below).

Table 1. Viscosity and diffusion coefficients used in the 1/12 global ocean simulation

Parameters	Values
Laplacian coefficient for momentum	20 m^2 s^{-1}
Biharmonic diffusive velocity for momentum	2 cm s^{-1}
Biharmonic diffusive velocity for layer thickness	2 cm s^{-1}
Laplacian diffusive velocity for tracers	0.5 cm s^{-1}

Although a detailed evaluation of the global ocean circulation and the sea ice is beyond the scope of this work, some basic measures are useful. Figure 2 displays the evolution of the domain averaged potential temperature and total kinetic energy of the world ocean. The model temperature exhibits a warming of ~0.02° C per decade (Figure 2a, domain-averaged salinity is constant because of the zero net freshwater flux constraint). The warming is induced by a positive net heat flux of ~1.2 W/m^2 (averaged over 1958-2015). This net heat flux in model is about twice the estimates of 0.50 (±0.43) W/m^2 based on the energy gain at the top of atmosphere for 2001-2010 (Loeb et al., 2012) and 0.64 (±0.11) W/m^2 based on 0-700 m oceanic heat content change from combined XBT and Argo data for 1993-2008 (Roemmich et al., 2015). However, the modeled net heat flux is within the range of 16 air-sea heat flux products based on global ocean/coupled reanalysis, which found an ensemble mean net heat flux of 1-2 W/m^2 in 1993-2009 (4.2±1.1 W/m^2 without data-assimilation) (Valdivieso et al., 2017). The modeled total kinetic energy spins up quickly to ~35 cm^2/s^2 in the first two years and remains on that level for the rest of the integration (Figure 2b). The global 1/10° simulation performed by Maltrud and McClean (2005) using the Parallel Ocean Program (POP) also reached a maximum in kinetic energy in the first couple of years, except that it is weaker and levels off at about 25-30 cm^2/s^2 (their Figure 1).

The sea ice is quantified and monitored in term of sea ice extent, defined as the area with 15% or higher sea ice concentration. Figure 3 compares the evolution of the modeled sea ice extent in million km^2 with the updated results from the National Snow and Ice Data Center (Fetterer et al., 2017). There is a general agreement between model and data in both the northern and southern hemispheres and on both seasonal (Figure 3a) and interannual (Figure 3b) timescales. In particular, as in the observations, the modeled sea ice extent has been decreasing in the northern hemisphere since the beginning of the observations in 1979 (note that the pace of the decline is slightly slower in the model). The modeled sea ice extent in the southern hemisphere is relatively stable or increases slightly over time and is in good agreement with the observations (Figure 3b).

Figure 4 shows the modeled AMOC transport at 26.5°N, defined as the northward trans-basin transport above the modeled time mean maximum overturning depth (1000 m). The modeled AMOC transport starts at 15 Sv and exhibits a decreasing trend of 0.43 Sv per decade (Figure 4a) with a mean value of 12.2 Sv in 2004-2015. The latter value is 4.6 Sv or ~30% lower than the 16.8 Sv based on the RAPID data (e.g., McCarthy et al., 2015). A similar low AMOC transport of 12.4 Sv is also found in a 1/12° global ocean simulation using the same atmospheric forcing over the same time period but with a different ocean model, i.e. NEMO (Blaker et al., 2015). The low AMOC may therefore be due to our choice of atmospheric forcing. The modeled AMOC variability, however, compares well to the RAPID observations, with a standard deviation value of 3.2 and 3.4 Sv, respectively, for the modeled and observed monthly mean transports in 2004-2015 (Figure 4b). The magnitude of the modeled interannual variability is slightly lower than observed, with a standard deviation of 1.0 Sv versus 1.5 Sv for the annual mean transports (Figure 4b). On seasonal timescales, the modeled AMOC variability is similar to observations in both magnitude (multi-year averaged monthly mean transports give a standard deviation of 1.6 Sv) and phase, with low transports in January-June and high transports in July-December (Figure 4c).

3. Modeled and observed circulation in the South Atlantic

In this section, we first compare the large-scale surface circulation to observations, and then examine in more detail the transport structure along three sections in the South Atlantic: 34°S, 65°W in the Drake Passage, and a Prime Meridian-Good Hope section southwest of Africa (Figure 1). Significant observations have been conducted at these locations and they provide an important benchmark for evaluating the realism of the modeled transports, which are used to document the transport structure of the South Atlantic.

3.1 The surface circulation pattern

Figure 5 compares the observed and modeled mean sea surface height (SSH), SSH variability, and eddy kinetic energy (EKE) of the surface currents in the South Atlantic. The observed mean SSH (Figure 5a) is from the climatology CNES-CLS13 (Rio et al., 2014) while the SSH variability (Figure 5c) and surface EKE (Figure 5e) are derived from the AVISO data over 1993-2012, the same time period used for model results. In the western side of the domain, part of the Antarctic Circumpolar Current (ACC) turns north after passing the Drake Passage and becomes the Malvinas Current (also called the Falkland Current). The latter continues to flow northward along the continental shelf of Argentina until it meets the southward flowing Brazil Current south of the Rio de la Plata estuary near 36°S. The confluence of these two western boundary currents with opposite directions and very different properties (warm salty subtropical water versus cold fresh subantarctic water) leads to numerous high-energy eddies and thus strong variability in this so-called Brazil-Malvinas confluence zone (Figures 5c-f). In the south, the ACC is mostly zonal and exhibits a contracted (stronger) front in two areas: one near 40°W south of the Zapiola Drift and the other near 10°W over the MAR. We note that the model results are in good agreement with the observations.

West of Africa, the numerical model exhibits a tongue of high SSH variability/EKE that extends farther into the South Atlantic than is seen in observations. This is a common feature for many eddying models (e.g., Maltrud and McClean, 2005; Dong et al. 2011) where the Agulhas rings that shed from the Agulhas retroflection and translate northwestward into the South Atlantic follow a regular pathway and are too energetic. Figure 6 further illustrates this, showing the SSH variability for both the model and the observations along the Prime Meridian over the 10-year period of 2003-2012. The figure shows that the modeled rings are stronger and pass this longitude within a smaller latitudinal range than is seen in the observations.

3.2 The Meridional Circulation across 34°S

To discuss the circulation/transport structure, we first examine the distribution of key water masses in this region. Figure 7 displays a vertical section of the mean potential temperature θ and salinity S at 34°S. The observations are based on the gridded monthly Argo profiles (2004-2014) for the upper 2000 m and the World Ocean Atlas 2013 (WOA13, Locarnini et al. 2013; Zweng et al. 2013) below 2000 m; the model results are 35-year means (1981-2015). The water column at this latitude can be divided into four density layers of water masses that are characterized most clearly in salinity (θ decreases monotonically): saline near surface water ($\sigma_2<35.65$ kg m^{-3}), fresh Antarctic Intermediate Water (AAIW, $35.65<\sigma_2<36.58$), saline NADW ($36.58<\sigma_2<37.12$), and fresh Antarctic Bottom Water (AABW, $\sigma_2>37.12$). There is a general agreement in the temperature and salinity distributions, although the salinity values differ somewhat between the model and observations (e.g., fresher AAIW in the observations).

The time mean meridional velocity across 34°S and the corresponding volume transports for the four water masses defined above are shown in Figure 8. The observations consist of geostrophic transports derived from θ/S profiles (Argo-WOA13 data) and Ekman transports from the wind stress; see Dong et al. (2014) for details. The model results are 35-year means (1981-2015). The main circulation at this latitude consists of the South Atlantic subtropical gyre (southward Brazil Current near the western boundary and northward interior flow) and the AMOC (northward Bengula Current near the eastern boundary and southward DWBC near the western boundary). Quantitatively, the modeled southward western boundary current is about 50 Sv (15, 10, and 25 Sv for the surface water, AAIW, and NADW, respectively), compared to 45 Sv observed (7, 8, and 30 Sv for the surface water, AAIW, and NADW, respectively). In the observations, the subtropical gyre in the surface water and AAIW layers extends from the western boundary to ~10°E, while the northward flow of the AMOC component occupies the rest of the section from ~10°E to the coast of Africa. The modeled transport pattern is similar to the observations, except that the regular pathway of the Agulhas rings leads to a north/south circulation in the Cape Basin. In the NADW layer, both observations and model results show a strong southward DWBC west of 40°W and a northward return flow east of 40°W. Note that the DWBC is quite wide at this latitude and that the transport obtained by Meinen et al. (2017), 15 Sv west of 44.5°W, does not include the full DWBC (30 Sv in Argo-WOA13 based observations and 25 Sv in model). The return flow is distributed over a wide region between 40°W and 0°E in model whereas it is more localized over the Walvis Ridge in the observations. In the Cape Basin, both observations and model results show a recirculation of the NADW. This recirculation is likely driven by eddy activity in the upper ocean and is stronger in the model (see Figure 5). The modeled AABW transport is 1 Sv in the western basin, much less than the 4-7 Sv estimated in observations (e.g., Hogg et al., 1982; Speer and Zenk, 1993). There is no northward AABW transport in the Argo-WOA13 based results.

The meridional flows in Figure 8 show significant barotropic components, and the baroclinic nature of the AMOC, i.e., northward flows in the upper limb and southward flows in the lower limb, becomes apparent only when integrated across the basin (Figure 9). The zonally-integrated mean transport stream functions with respect to depth *z* show a maximum overturning depth of ~1300 m in both observations and model results (Figure 9a). The modeled mean AMOC transport is 14 Sv. This value is in good agreement with the latest estimate based on six years of moored observations at the western and eastern boundaries (14.7 Sv, Meinen et al., 2018), but is significantly lower than the estimates based on XBT transects (18 Sv, Dong et al., 2009; Garzoli et al., 2013) and Argo-WOA13 (20 Sv, Dong et al., 2014). With respect to density (Figure 9b), the northward limb is above the density surface (σ_2) 36.58 kg/m^3 and the southward limb below. The modeled mean AMOC transport is 15.3 Sv, compared to 18.7 Sv based on Argo-WOA13 (18.1 Sv based on XBT transects). The modeled northward limb consists of 9.6 Sv of warm surface water transport and 5.7 Sv of AAIW transport, compared to 12.7 and 6.0 Sv, respectively, in the observations. This implies a lower meridional heat transport (MHT) of 0.35±0.23 PW in the model, compared to 0.68±0.24 PW in the Argo-WOA13 results. The historical estimates of the MHT near this latitude are 0.22-0.62 PW (see Table 29.3 in Macdonald and Baringer, 2013).

The modeled AMOC transport variability is also lower than in the Argo-WOA13 based observations, on both interannual and seasonal timescales (Figure 10): In 2004-2014, the modeled annual mean transports have a standard deviation of 0.7 Sv, compared to 2.0 Sv in observations (Figure 10a); the 11-year averaged monthly mean transports have a standard deviation of 2.3 Sv in the model, compared to 3.3 Sv in observations (Figure 10b). Although the magnitude is lower, the phase of the modeled seasonal variability is consistent with the observations (Figure 10b).

3.3 ACC Transport through the Drake Passage at 65°W

The Drake Passage is the narrowest constriction of the ACC in the Southern Ocean and the place where long-term sustained monitoring programs have been conducted; see Meredith et al. (2011) for a review of historical observations. The canonical full-depth volume transport is 133.8 ±11.2 Sv, based on year-long mooring and cruise data obtained during the International Southern Ocean Studies (ISOS, Whitworth, 1983; Whitworth and Peterson, 1985). Using a 20-year transport time series based on satellite altimetry data (1992–2012) and in situ current meter data (2006-2009), this value was increased by Koenig et al. (2014) to 141 Sv, with a standard deviation of 13 Sv and an error estimate of 2.7 Sv. More recently, Chidichimo et al. (2014) and Donohue et al., (2016), estimated a significantly higher mean ACC transport of 173.3 Sv (primarily due to a higher barotropic component) based on high-resolution moored observations from 2007 to 2011.

In the model, the mean ACC transport is 155.5 Sv, in line with the observations. The modeled mean zonal velocity through the Drake Passage at 65°W and the corresponding volume transports for the four density layers defined earlier (surface water, AAIW, NADW, AABW) are shown in Figure 11a. The ACC at this longitude exhibits four high velocity cores (indicated by arrows in Figure 11a), corresponding to the ACC southern boundary (SBby, south of 63°S), the southern ACC Front (SACCF, at 61-62°S), the Polar Front (PF, at 58-60°S), and the Sub-Antarctic Front (SAF, at 55-55°S). These modeled fronts are at the same locations as in the classical description of Orsi et al. (1995) based on hydrographic surveys and as in the more recent results of Firing et al. (2011) using 4.5 years of shipboard ADCP (acoustic Doppler current profiler) surveys; note the SAF is wide in Figure 11a because the front turns northward at this longitude.

To examine the vertical structure, the modeled ACC transport at 65°W is shown in green in Figure 12a. At that longitude, the modeled ACC transport decreases exponentially with depth, as in the observations of Firing et al. (2011). In the top 1000 m, the modeled ACC transport is 89 Sv, which is close to the 95 Sv in Firing et al. (2011) and the 90 Sv in Donohue et al. (2016). One can further break down the transport into baroclinic and barotropic components: at 65°W and above 3000 m, the modeled total, baroclinic, and barotropic transports are 149.4, 112.7, and 36.7 Sv, respectively, compared to the observed 140, 112, and 28 Sv in Koenig et al. (2014). Thus, the modeled ACC transport is higher than in Koenig et al. (2014) because of a stronger barotropic component contribution. Note that the higher total ACC transport obtained in Donohue et al. (2016) is also due to a higher barotropic contribution (45.6 Sv). Overall, the barotropic component remains the main uncertainty in determining the total ACC transport.

The modeled monthly mean and annual mean ACC transports have a standard deviation of 5.2 Sv and 2.1 Sv, respectively (Figure 13a). These numbers are relatively small compared to the long-term mean value of ~155 Sv. The seasonal variability is also small (with a standard deviation of 1.3 Sv) and exhibits a biannual pattern of high transports in April and October and low transports in June and January (Figure 13b). These results agree with Koenig et al. (2016).

3.4 Zonal transports south of Africa

The wide ocean gap between the Antarctica and southern tip of Africa makes it difficult to fully measure the transport and its spatial structure. Observations have mostly focused on measurements along the Prime Meridian (e.g., Whitworth and Nowlin 1987; Klatt et al. 2005) to approximately 50°S and the Good Hope line from 0°E, 50°S to the Cape of Good Hope, South Africa (e.g., Legeais et al. 2005; Gladyshev et al. 2008; Swart et al. 2008). We refer to the combination of these two sections as the Prime Meridian-Good Hope (PM-GH) transect (Figure 1), along which the velocity/transport structure is examined. The modeled net transport through PM-GH (156.5 Sv) is essentially the same as the net transport through the Drake Passage because of mass conservation, except for an additional 1 Sv from the Pacific-to-Atlantic Bering Strait throughflow.

The circulation along the PM-GH section can be divided into three regimes (Figure 11b):

i) Weddell gyre south of 55.5°S. There are two eastward and two westward jets that form the Weddell gyre. The two westward jets are found along the Antarctic Slope and the Maud Rise (MR) near 64°S, whereas the two eastward jets are found near 58-59°S and along the southern boundary (SBdy) of the ACC at 55.5°S right south of the Southwest Indian Ridge (SIR). This jet pattern is consistent with the observations of Klatt et al., (2005, their Figures 4-5). The time mean transport of the modeled Weddell gyre is 47.1 Sv, compared to 55.7 Sv in Klatt et al. (2005).

ii) ACC from 55.5 to 40°S. The modeled ACC exhibits high-velocity cores associated with the SACCF (52°S), PF (50.4°S and 48°S), SAF (44.6°S), and the subtropical front (STF, 42°S) respectively. These front positions are close to the observations based on repeat CTD/XBT transects in this region (Swart et al. 2008, their Table 3). Note that the PF at this location is split into two fronts, with the elevated eastward velocity between 47°S and 49°S corresponding to its northern expression (Swart et al. 2008; Gladyshev et al. 2008). The modeled STF is much weaker than any of the other ACC fronts as in the observations. The modeled mean ACC transport across the PM-GH transect, defined as the transport from 55.5 to 40°S including the STF as in Orsi et al., (1995), is 177 Sv, compared to 147-162 Sv estimated from CTD transects (Whitworth and Nowlin, 1987, Legeais et al., 2005, Gladyshev et al., 2008). The modeled baroclinic transport is 106.4 Sv above 2500 m, compared to 84.7-97.5 Sv derived from repeated hydrographic surveys and in combination with satellite altimetry data (Legeais et al. 2005; Swart et al. 2008).

iii) Agulhas retroflection and leakage north of 40°S. Farther north, the model results show a pair of eastward and westward flows associated with the Agulhas retroflection and Agulhas Current. The 'net' transports north of 40°S is 12.0 and 9.4 Sv westward for the surface water and AAIW. Thus, the Agulhas leakage provides more transport than the upper AMOC (~ 7 Sv return eastward in the STF).

The modeled transport across the full PM-GH transect decreases with depth and is eastward above 4000 m (blue line in Figure 12a). There is a weak westward flow below 4000 m. When compared to the vertical structure of the transport in the Drake Passage (green line in Figure 12a), the eastward transport through PM-GH transect is weaker in the 0-600 m range and stronger between 600 and 3500 m. The latter is due, in part, to the contribution of NADW transport from the lower limb of the AMOC (red line in Figure 12a).

The modeled net transports into and out of the region bounded by a) 34°S, b), Drake Passage, and c) PM-GH (see Figure1) is shown in Figure 12b. Between 1500 m and the bottom, there is a net positive inflow. This implies a strong upwelling across 1500 m with a maximum upward transport of 8.8 Sv. This is consistent with the picture put forward by Schmitz (1995) and Talley (2013) that the Southern Ocean is a key upwelling region for NADW.

4. Large-scale time mean circulation in the South Atlantic Ocean

In the previous section, we showed that the model is able to represent the basic circulation features of the South Atlantic and the Southern Ocean with reasonable accuracy. In this section, we use the model results to further explore the time-mean circulation in the South Atlantic. In particular, we focus on a) the diapycnal water mass transformations associated with the upwelling as shown in the previous section, and b) the lateral circulation patterns of the upper and lower limbs of the AMOC.

4.1 Diapycnal water mass transformations

Similar to Figure 12b, Figure 14a shows the net transports into and out of the region bounded by the 34°S, 65°W, and PM-GH sections, but with respect to density layers. The positive transports (black) denote water flowing into the region which has to exit into another density layer flowing out of the region (white). A downward integration of these layered transports gives the net transport between the sea surface and a given density surface, and the difference between this net transport and the change of the volume above the density surface over time gives the total diapycnal water mass transformation (black line in Figure 14b) taking place in the region across that density surface; see Xu et al. (2018) for a more detailed discussion on water mass transformation.

The results (black line in Figure 14b) show that there are transformations of intermediate water (34.50-35.92 range) in this region: ~10 Sv from denser water across the density surface of 35.92 and ~6 Sv from lighter water across 34.50. The diapycnal transformation can be compared to the transformation (dashed black line in Figure 14b) that is driven directly by the surface buoyancy fluxes, calculated from the surface density fluxes and surface density using the thermodynamic method (e.g., Walin 1982; Speer and Tziperman, 1992; Brambilla et al., 2008; Langehaug et al., 2012; Xu et al., 2018). The result suggests that the surface-forced transformation accounts for most of the area-integrated diapycnal transformation in the South Atlantic region bounded by the three sections. Spatial distribution of the transformation (not shown) further supports the notion that the diapycnal transformation in this region is mostly due to surface buoyancy forcing: the ocean loss buoyancy in the Agulhas Leakage region and the Brazil-Malvinas confluence zone, and gain buoyancy in the ACC.

4.2 AMOC horizontal circulation patterns

a) Upper limb (surface water and AAIW)

The upper (northward) limb of the AMOC consists of two density layers: the surface water (σ_2<35.65) and the AAIW (35.65<σ_2<36.58 kg m^{-3}). The modeled 35-year (1981-2015) mean horizontal circulation for these two layers is displayed in Figures 15 and 16, respectively. There are three distinct pathways for the surface water (Figure 15): first, the AMOC component which flows directly northwestward (the so-called Agulhas Leakage) into the

South Atlantic (red stream lines); second, the subtropical 'supergyre' that flows around the subtropical gyre and connects the South Atlantic and Indian Ocean (De Ruijter, 1982; Gordon 1992) (blue lines); and third, the subtropical gyre (orange lines). There is virtually no surface water in the ACC from the Pacific Ocean (pink lines). In addition, this surface water is prevented from moving north in the South Atlantic because of the 'supergyre' and cannot contribute directly to the AMOC.

The circulation pattern of the modeled AAIW (Figure 16) is similar to the surface water (Figure 15), but it shows a meridionally more confined subtropical gyre (orange lines) and a larger contribution to the ACC from the Pacific Ocean (pink lines). As for the surface water, there is a 'supergyre' connecting the subtropical gyres of the South Atlantic and Indian Oceans, which prevents a direct contribution of water mass from the ACC into the upper limb of the AMOC. The modeled circulation patterns of Figures 15 and 16 are similar to the schematic of Stramma and England (1999, their Figures 3-4) except for the recirculation in the Cape Basin, which is due to the unrealistic pathways of the modeled Agulhas eddies (see Figures 5 and 6 and discussion in section 3.1).

Although the AAIW in the ACC does not directly contribute to the upper limb of the AMOC, the cold Pacific water entering the South Atlantic via the Drake Passage does play a role in setting the subtropical gyre water mass characteristics. To illustrate this, we project the northward volume transports across the 45°S, the 34°S, and the GH sections (Figure 16) in terms of potential temperature and salinity (θ-S). The results show a) the Pacific AAIW (35.65-36.58) that flows northward across 45°S (Figure 17a) is much colder and fresher than the Indian AAIW that flows westward across the GH section (Figure 17c); and b) the AAIW that flows northward across 34°S (Figure 17b) is a combination of these two water masses. About 9.2 Sv of the northward AAIW transport across 34°S exhibit properties similar to the warmer saltier Indian water at the GH section, whereas about 8.3 Sv exhibit properties similar to the colder fresher Pacific water at 45°S. Thus, although the cold Pacific water does not directly feed into the upper limb of the AMOC, it contributes to the water properties at 34°S and impacts the meridional heat/freshwater transports.

b) Lower limb (NADW)

Figure 18 shows the modeled mean circulation for the NADW density layer ($36.58<\sigma_2<37.12$). The modeled NADW flows southward as a DWBC along the continental slope of the Brazil and the Argentine Basins, all the way to about 40°S where it encounters the northward-flowing deep Falkland Current. The NADW continues to flow southward (now offshore of the deep Falkland Current) to about 45°S where it meanders and flows eastward south of the Zapiola Drift (Rise). This modeled NADW pathway is similar to the one described in the schematic of Stramma and England (1999, their Figure 5) and is consistent with picture derived from salinity, oxygen, and other tracers (CFC, for example) (e.g., Koltermann et al., 2011; Garzoli et al., 2015). There is a strong counter-clockwise flow around the Zapiola Drift (Figure 18). Within the NADW layer across 45°S, the modeled transport is about 45 Sv for the southward flow in the western side and 25 Sv for northward flow in the eastern side. For the full water column, the modeled long-term mean transport for this Zapiola anticyclone is on the order of 90 Sv in the western side and 50 Sv in the eastern side. Saunders and King (1995) proposed a flux of 80 Sv based on one CTD/ADCP survey along 45°S, but they cautioned that the feature is "unexpected and not entirely free from uncertainty." The model results suggest that their estimate actually may be quite reasonable.

Offshore of the DWBC, there are complex recirculation patterns in the Brazil Basin, especially around the Vitoria-Trindade Seamount Chain near 20°S (Hogg and Owens, 1999). The recirculation carries NADW from the DWBC toward the interior of the basin and explains the high salinity signature found along the WOCE lines A09 and A095 that extend all the way to the MAR in both the observations and the model (Figure 19). The model results exhibit a zonal flow of about 2 Sv across the MAR near 22°S (see Figure 20 over the bathymetry). This zonal flow has been the subject of a number of studies, with an estimated transport ranging from 2.2 to 5 Sv (i.e., Warren and Speer, 1991; Speer et al., 1995; Hogg and Thurnherr, 2005; Garzoli et al., 2015) although 10.7 Sv in Arhan et al. (2003). Note in Figure 19 that the salinity is similar between A15 and A16, but quite different between A15 and A14. The salinity contrast does not support a high transport across the MAR.

South of 22°S, there are weaker, more widespread westward zonal flows across the MAR (Figures 18 and 20). As a consequence, the interior salinity in the west basin near 30°S (along A10) is much lower compared to 20-25°S (A09 and A095). Also, the modeled net transport across the MAR is close to zero and virtually all the NADW flows across the MAR south of 40°S. As the NADW from north and the ACC water from the Drake Passage flow eastward, the streamlines turn northward when approaching the MAR and southward after crossing the MAR. This meridional shift can be explained by the conservation of potential vorticity, i.e., a decrease in thickness h when approaching the MAR leads to a northward shift to reduce the planetary rotation f so that f/h is constant and vice versa. Because the MAR is slanted in a northwest-to-southeast direction in this area, the northward and southward shifts at different longitude lead to a contraction of the front near 10°W, clearly visible in the SSH for both model and observations (Figure 5).

5. Latitudinal coherence of the AMOC variability

In this section, we examine whether the modeled AMOC variability is latitudinally coherent throughout the Atlantic from 35°S to 70°N. Using hydrography and satellite data with a box model, Kelly et al. (2014) suggest that the meridional heat transport anomalies (closely correlated with the strength of the AMOC) are highly coherent from 35°S to 40°N on interannual timescales. Xu et al. (2014) found a similar result, but their model was regional (did not extend past 25°S) and was only integrated for eight years after spin up. The model used in this study is global and was integrated for close to six decades. To examine the latitudinal coherence on different timescales, we focus on the last 35 years (1981-2015) of the simulation to ensure that the solution is fully spun up. First, we compute monthly mean AMOC transports at all latitudes from 35°S to 70°N (in 0.5° increments) and then decompose the transport time series into different timescales using the ensemble empirical mode decomposition (EEMD, Wu and Huang, 2009). The EEMD extracts the amplitude-frequency modulated oscillatory components (termed as "intrinsic mode functions", or IMFs) successively from the highest to the lowest frequencies, without using a priori determined basis function. The advantage of this method is that both the frequency and amplitude of each IMF are determined adaptively from the local characteristic of the time series and vary as a function of time. Finally, the same IMF at each latitude is pieced together to construct the basin-scale AMOC variability.

The number of IMFs is the integer of the binary logarithm of the time series length N (log_2N), or 7 for N=420 months. The first two IMFs represent the high-frequency intraseasonal variability and are not shown. The third IMF (Figure 21) exhibits frequency close to seasonal timescale. The results show that the seasonal AMOC variability is high, especially in the equatorial region due to the seasonal migration of the Inter-tropical convergence zone (ITCZ), and is coherent across different latitudes. To the south and north of about 20°N, there is a shift in the phase of the variability. These results are very similar to the regional Atlantic model of Xu et al. (2014). The phase shift seen in the model can also be seen in observations: for example, high seasonal AMOC transports occur during April-August at 34°S (Figure 10b based on Argo-WOA13 data), compared to July-November at 26.5°N (Figure 4c based on RAPID data).

The fourth and fifth IMFs are presented in Figure 22 and they represent interannual variability. The interannual variability is weaker than seasonal variability; it also exhibits a good coherence throughout the Atlantic domain. Near 40°N, there is a phase shift with variability in the subpolar North Atlantic leading the variability in the subtropics. This shift is clearer in the fifth IMF (Figure 23b). South of 35°N, the interannual variability is very similar in phase and is consistent with the finding of Kelly et al. (2014) based on observations, i.e., that the interannual variability of the meridional heat transport (a good index for AMOC) is highly coherent between 35°S and 40°N on these timescales.

The sixth and seventh IMFs (Figure 23) represent the AMOC variability on decadal (about 10-30 years) timescales. The decadal variability is even weaker than interannual timescales and exhibits a good coherence. Similar to the interannual variability shown in Figure 22b, the decadal variability in Figure 23a (10-year) shows a phase shift near 40°N with variability of the subpolar North Atlantic leading variability farther south. The variability in Figure 23b generally shows a high AMOC transport period from 1985-2000 and a lower AMOC transport from 2000-2015, a close to 30-year variation that is coherent from 35°S to 50°N.

6. Summary and Discussion

Through the South Atlantic Ocean, the AMOC is connected to the Indian and Pacific Oceans and is entangled into the global overturning circulation system. This important region is also particularly complex, featuring strong boundary currents (jets) and high eddy variability in both the western and eastern boundaries as well to the south in the Atlantic sector of the Southern Ocean. Observations of the full-depth circulation structure are focused on limited places, thus the 3-D circulation structure in the South Atlantic and the large-scale pattern of the AMOC variability are not well-determined. In this study, we used numerical results from a long-term 1/12° global simulation, along with observations, to address the fundamental questions. The model results are shown to represent the transports and the vertical structure of the key circulation patterns in this region, especially, the AMOC across 34°S in the South Atlantic, the ACC at 65°W in the Drake Passage, as well as the zonal flows along the PM-GH transect in the open ocean southwest of Africa. The key results are

1) Strong upwelling takes place in the South Atlantic Ocean. In the area south of 34°S between the Drake Passage (65°W) and southwest of Africa (PM-GH), there is a maximum upward transport of 8.8 Sv across 1500 m. The water in this area also undergoes a strong diapycnal transformation that forms about 16 Sv intermediate water in 34.50-35.92 density range: 10 Sv from denser AAIW and NADW and 6 Sv from lighter near surface water.

2) In the upper limb of the AMOC, the northward flow originates from the warm Agulhas leakage. The existence of a super gyre (connecting the subtropical gyre of Atlantic and Indian Oceans) prevents the colder fresher Pacific water from directly contributing to the AMOC. The cold water, however, modifies the water properties of both the AMOC and the subtropical gyre across 34°S, thus contributing to the meridional transports of heat and freshwater (salinity anomaly).

3) In the lower limb, the NADW flows southward in the DWBC along the continental slope and in complex recirculation in the Brazil Basin, especially around the Vitória-Trindade Seamount Chain near 20°S. The recirculation carries the NADW and its high-salinity signature into the offshore interior. A zonal flow of NADW crossing the MAR is found near 22°S. This zonal flow is likely minor given the fact that the salinity/oxygen east of MAR is significantly lower as compared to the west. Virtually all of the NADW from the north flows in the DWBC all the way to 40-45°S before turning eastward to flow across the MAR near 42°S. The location of this crossing can be seen as a contracted ACC front near 10°W.

4) Overall, the modeled AMOC variability from seasonal to decadal timescales (Figure 21-23) shows a good meridional coherence throughout the Atlantic Ocean, especially from 35°S to about 35°N, consistent with the finding by Kelly et al. (2014). The coherence in this latitude range, where the diapycnal water mass transformation between the upper and lower AMOC limbs is expected to be small, indicates that the AMOC variability is modulated by deep water formation in the subpolar North Atlantic and/or upwelling regions. The decadal variability shows some phase shift near 40°N, with variability of the subpolar North Atlantic leading that to the south. A similar phase shift near this latitude is found in the coupled climate

simulation of Zhang (2010), but not robust across in the coupled CMIP5 and in the atmospherically-forced global ocean-sea ice simulations at similar resolution, i.e., the CORE-II (Xu et al. 2018b).

Some model features need to be improved. One key challenge for numerical models in this region is to represent the northwestward translation of the Agulhas rings into the South Atlantic. Compared to observations, the modeled rings are dissipated slower and follow a more regular pathway. This leads to a high EKE tongue extending much farther to the northwest and has significant impact on the regional circulation pattern in the eastern South Atlantic. Possible improvements may result from a) including the ocean currents in the wind stress calculation, which adds a significant damping effect to eddies (Renault et al., 2017); and b) using a higher order advection scheme in momentum equation, which leads to more irregularity in eddy size and pathway (Backeberg et al., 2009).

Furthermore, the results presented in this study are based on a single simulation so the robustness needs to be examined with coordinated model comparison efforts, with the same model resolution and atmospheric forcing. Such multi-model inter-comparison efforts have been shown to be useful in the low-resolution, atmospherically-forced global ocean-sea ice simulations under the CORE-II and the fully-coupled climate simulations under CMIP5 (e.g., Xu et al., 2018b). A similar effort with several ocean general circulation models (OGCMs) at 1/12° resolution, all using the latest atmospheric forcing JRA-55 (Tsujino et al., 2018), is ongoing and the robustness of the modeled circulation in this important region will be further investigated.

Acknowledgement: The work is supported by NOAA-Earth System Prediction Capability Project (Award NA15OAR4320064), NOAA Climate Program Office MAPP Program (Award NA15OAR4310088), and Climate Variability and Predictability Program (Award GC16-210), and NOAA's Atlantic Oceanographic and Meteorological Laboratory. The numerical simulations were performed on supercomputers at the Navy DoD Supercomputing Resource Center, Stennis Space Center, Mississippi, using computer time provided by the U.S. DoD High Performance Computing Modernization Program. The sea ice extent data are available from National Snow & Ice data Center (https://nsidc.org/data); the altimeter products used here were produced by Ssalto/Duacs and distributed AVISO, with support from CNES http://www.aviso.altimetry.fr/duacs; the gridded T/S fields from the Argo float measurements are available at http://www.argo.ucsd.edu/Gridded_fields.html and the World Ocean Atlas 2013 is available at http://www.nodc.noaa.gov/OC5/woa13; the velocity at 1000 m is obtained from http://apdrc.soest.hawaii.edu/projects/Argo/data/trjctry; the global model outputs are stored in the U.S. Navy DSRC archive server and the model results presented in this study are available in HYCOM server (ftp://ftp.hycom.org/pub/xbxu/GLBb0.08/SATL).

Reference:

Arhan, M., Mercier H., & Park Y.-H. (2003). On the deep water circulation of the eastern South Atlantic Ocean. *Deep-Sea Research Part I*, **50**, 889–916.

Backeberg, B.C., Bertino, L., & Johannessen, J.A. (2009). Evaluating two numerical advection schemes in HYCOM for eddy-resolving modelling of the Agulhas Current, *Ocean Science*, 5, 173-190, https://doi.org/10.5194/os-5-173-2009

Baringer, O. M., & Garzoli, S. L. (2007). Meridional heat transport determined with expendable bathythermographs. Part I: Error estimates from model and hydrographic data. *Deep-Sea Research Part I*, **54**, 1390–1401.

Beal, L. M., W. P. M. De Ruijter, A. Biastoch, R. Zahn, and SCOR/WCRP/IAPSO Working Group 136 (2011), On the role of the Agulhas system in ocean circulation and climate, *Nature*, **472**(7344), 429–436, https://doi.org/10.1038/nature09983

Blaker, A.T., Hirschi, J.J.-M., McCarthy, G.D., Sinha, B., Taws, S.L., Marsh R., et al. (2015). Historical analogues of the recent extreme minima observed in the Atlantic meridional overturning circulation at 26°N. *Climate Dynamics*, **44**, 457–473, https://doi.org/10.1007/s00382-014-2274-6

Bleck, R. (2002). An oceanic general circulation model framed in hybrid isopycnic-Cartesian coordinates. *Ocean Modelling*, **37**, 55–88.

Brambilla, E., Talley, L. D. & Robbins, P. E. (2008). Subpolar Mode Water in the northeastern Atlantic: 2. Origin and transformation. *Journal of Geophysical Research-Oceans*, **113**(C4). https://doi.org/10.1029/ 2006JC004063

Broeker, W. S. 1991. The great ocean conveyor. *Oceanography* **4**(2):79–89.

Carnes, M. R. (2009). Description and evaluation of GDEM-V3.0. Tech. Rep. NRL/MR/7330–09–9165, 21 pp., Naval Res. Lab, Stennis Space Center, Miss.

Chassignet, E. P., Smith, L. T., Halliwell, G. R. & Bleck, R. (2003). North Atlantic simulations with the hybrid coordinate ocean model (HYCOM): Impact of the vertical coordinate choice, reference pressure, and thermobaricity. *Journal of Physical Oceanography*, **33**, 2504–2526.

Chassignet, E. P., Hurlburt, H. E., Smedstad, O. M., Halliwell, G. R., Wallcraft, A. J., Metzger, E. J., et al. (2006). Generalized vertical coordinates for eddy-resolving global and coastal ocean forecasts, *Oceanography*, **19**(1), 20–31. https://doi.org/10.5670/oceanog.2006.95

Chassignet, E. P. & Xu, X. (2017), Impact of horizontal resolution (1/12° to 1/50°) on Gulf Stream separation, penetration, and variability, *Journal of Physical Oceanography*, **47**(08), 1999-2021, https://doi.org/10.1175/JPOD-17-0031.1

Chidichimo, M. P., Donohue, K. A., Watts, D. R., & Tracey, K. L. (2014). Baroclinic transport time series of the Antarctic Circumpolar Current measured in Drake Passage, *Journal of Physical Oceanography*, **44**(7), 1829–1853.

Cunningham, S. A., Alderson, S. G., King, B. A., & Brandon M. A. (2003). Transport and variability of the Antarctic Circumpolar Current in Drake Passage, *Journal of Geophysical Research-Oceans*, **108**(C5), 8084, https://doi.org/10.1029/2001JC001147.

Dussin, R. B., Barnier, L. Brodeau, & Molines, J. M. (2016). The making of the DRAKKAR forcing set DFS5. DRAKKAR/MyOcean Report 01-04-16.

Dong, S., Garzoli, S., Baringer, M., Meinen, C., & Goni, G. (2009). Interannual variations in the Atlantic meridional overturning circulation and its relationship with the net northward heat transport in the South Atlantic. *Geophysical Research Letter*, **36**, L20606, https://doi.org/10.1029/2009GL039356.

Dong, S., Garzoli, S., & Baringer, M. (2011). The Role of inter-ocean exchanges on decadal variations of the meridional heat transport in the South Atlantic. *Journal of Physical Oceanography*, **41**, 1498–1511.

Dong, S., Baringer, M. O., Goni, G. J. Meinen, C. S., & Garzoli, S. L. (2014). Seasonal variations in the South Atlantic meridional overturning circulation from observations and numerical models, *Geophysical Research Letter*, **41**, 4611–4618, https://doi.org/10.1002/2014GL060428

Dong, S., Goni, G., & Bringas, F. (2015). Temporal variability of the South Atlantic Meridional Overturning Circulation between 20°S and 35°S, *Geophysical Research Letter*, **42**, 7655–7662, https://doi.org/10.1002/2015GL065603.

Donohue, K. A., Tracey, K. L., Watts, D. R., Chidichimo, M. P., & Chereskin, T. K. (2016). Mean Antarctic Circumpolar Current transport measured in Drake Passage. *Geophysical Research Letters*, **43**, 11760–11767. https://doi.org/10.1002/2016GL070319

Fetterer, F., Knowles, K., Meier, W., Savoie, M., & Windnagel. A. K. (2017). Sea Ice Index, Version 3. Boulder, Colorado USA. NSIDC: National Snow and Ice Data Center. http://dx.doi.org/10.7265/N5K072F8.

Firing, Y. L., Chereskin, T. K., & Mazloff, M. R. (2011). Vertical structure and transport of the Antarctic Circumpolar Current in Drake Passage from direct velocity observations, *Journal of Geophysical Research-Oceans*, **116**, https://doi.org/10.1029/2011JC006999

Garzoli, S. L., & Matano, R. (2011). The South Atlantic and the Atlantic Meridional Overturning Circulation. *Deep-Sea Research Part II* **58**(17-18), 1837–1847. https://doi.org/10.1016/j.dsr2.2010.10.063.

Garzoli, S. L., Baringer, M. O., Dong, S., Perez, R. C., & Yao, Q. (2013). South Atlantic meridional fluxes, *Deep-Sea Research Part I*, **71**, 21–32, https://doi.org/10.1016/j.dsr.2012.09.003.

Garzoli, S. L., Dong, S., Fine, R., Meinen, C. S., Perez, R. C., Schmid, C., et al. (2015). The fate of the Deep Western Boundary Current in the South Atlantic, *Deep-Sea Research Part I*, **103**, 125–136, https://doi.org/10.1016/j.dsr.2015.05.008.

Gladyshev, S., Arhan, M., Sokov, A., & Speich S. (2008). A hydrographic section from South Africa to the southern limit of the Antarctic Circumpolar Current at the Greenwich meridian, *Deep-Sea Research Part I*, **55**, 1284–1303, https://doi.org/10.1016/j.dsr.2008.05.009.

Goes, M., Goni, G. & Dong, S. (2015). An optimal XBT-based monitoring system for the South Atlantic meridional overturning circulation at 34S, *Journal of Geophysical Research-Oceans*, **120**, 161–181, https://doi.org/10.1002/2014JC010202.

Gordon, A. L. (1986). Interocean exchange of thermocline water, *Journal of Geophysical Research-Oceans*, **91**(C4), 5037–5046, https://doi.org/10.1029/JC091iC04p05037.

Gordon, A.L. (2001). Interocean Exchange. Chapter 4.7. pp. 303–314 in *Ocean Circulation and Climate*, G. Siedler, J. Church, and J. Gould, eds. Academic Press.

Hogg, N. G., & Owens, W. B., 1999. Direct measurement of the deep circulation within the Brazil Basin. *Deep-Sea Research Part II.* **46**, 335–353. http://dx.doi.org/10.1029/2004/JC002311.

Hogg, N. G., & Thurnherr, A. M. (2005). A zonal pathway for NADW in the South Atlantic. *Journal of Oceanography*. **61**(3), 493–507.

Hogg, N. G., Biscaye, P. E., Gardner, W. D., & Schmitz, W. J. Jr. (1982). On the Transport and Modification of Antarctic Bottom Water in the Vema Channel, *Journal of Marine Research*, **40**, 231-263

Hunke, E. C., & Lipscomb, W. H. (2008). CICE: The Los Alamos sea ice model documentation and software user's manual, version 4.0, Tech. Rep. LA-CC-06-012, Los Alamos Natl. Lab., Los Alamos, N. M.

Kelly, K. A., Thompson, L., & Lyman, J. (2014). The coherence and impact of meridional heat transport anomalies in the Atlantic Ocean inferred from observations, *Journal of Climate*, **27**, 1469–1487, https://doi.org/10.1175/JCLI-D-12-00131.1.

Klatt, O., Fahrbach, E., Hoppeman, M. & Rohardt, G. (2005). The transport of the Weddell Gyre across the prime meridian, Deep-Sea Res., Part 2, 52, 513–528.

Koenig Z., Provost, C., Ferrari, R., Sennéchael, N., & Rio, M.-H. (2014). Volume transport of the Antarctic Circumpolar Current: Production and validation of a 20 year long times series obtained from in situ and satellite data, *Journal of Geophysical Research-Oceans*, **119**, 5407–5433, https://doi.org/10.1002/2014JC009966

Koenig, Z., Provost, C., Park, Y.-H., Ferrari, R., & Sennéchael, N. (2016). Anatomy of the Antarctic Circumpolar Current volume transports through Drake Passage, *Journal of Geophysical Research-Oceans*, **121**, 2572–2595, https://doi.org/10.1002/2015JC011436.

Koltermann, K.P., Gouretski, V.V. & Jancke, K. (2011). Hydrographic Atlas of the World Ocean Circulation Experiment (WOCE). Volume 3: Atlantic Ocean (eds. M. Sparrow, P. Chapman and J. Gould). International WOCE Project Office, Southampton, UK, ISBN 090417557X.

Langehaug, H.R., Rhines, P.B., Eldevik, T., Mignot, J., & Lohmann, K. (2012). Water mass transformation and the North Atlantic Current in three multicentury climate model simulations. *Journal of Geophysical Research-Oceans*, **117**(C11). https://doi.org/10.1029/2012JC008021

Large, W. G., & Yeager S. (2004). Diurnal to decadal global forcing for ocean and sea-ice models: The data sets and flux climatologies. NCAR Tech. Note NCAR/TN 460+STR.

Legeais, J. F., S. Speich, M. Arhan, I. J. Ansorge, E. Fahrbach, S. Garzoli, & A. Klepikov (2005). The baroclinic transport of the Antarctic Circumpolar Current south of Africa, *Geophysical Research Letter*, **32**, L24602, https://doi.org/10.1029/2005GL023271.

Locarnini, R. A., Mishonov, A. V., Antonov, J. I., Boyer, T. P., Garcia, H. E., Baranova, O. K., et al. (2013). Temperature. Vol. 1, World Ocean Atlas 2013, S. Levitus, Ed., A. Mishonov Technical Ed.; NOAA Atlas NESDIS 73, 40 pp.

Loeb, N. G., Lyman, J. M., Johnson, G. C. Allan, R. P., Doelling, D. R., Wong, T., et al. (2012). Observed changes in top-of-the-atmosphere radiation and upper-ocean heating consistent within uncertainty, *Nature Geoscience*, **5**, 110–113, doi:10.1038/NGEO1375

Macdonald, A. M., & Baringer, M. O., (2013). Ocean heat transport. In *Ocean Circulation and Climate: A 21st Century Perspective*, G. Siedler et al., Eds., International Geophysics Series, **103**, Academic Press, 759–786, https://doi.org/10.1016/ B978-0-12-391851-2.00029-5.

Maltrud, E.M., & McClean, J. (2005) An Eddy Resolving Global 1/10 Ocean Simulation. *Ocean Modelling*, **8**, 31-54. http://dx.doi.org/10.1016/j.ocemod.2003.12.001

McCarthy, G. D., Smeed, D. A., Johns, W. E., Frajka-Williams, E., Moat, B. I., Rayner, D., et al. (2015). Measuring the Atlantic meridional overturning circulation at 26ºN. *Progress in Oceanography*, **130**, 91–111, https://doi.org/10.1016/j.pocean.2014.10.006

Meinen, C. S., Speich, S., Perez, R. C., Dong, S., Piola, A. R., Garzoli, S. L., et al. (2013). Temporal variability of the Meridional Overturning Circulation at 34.5ºS: Results from two pilot boundary arrays in the South Atlantic, *Journal of Geophysical Research-Oceans*, **118**, 6461–6478, https://doi.org/10.1002/2013JC009228.

Meinen, C. S., Speich, S., Piola, A. R., Ansorge, I., Campos, E., Kersalé, M., et al. (2018). Meridional Overturning Circulation transport variability at 34.5ºS during 2009–2017:

Baroclinic and barotropic flows and the dueling influence of the boundaries, *Geophysical Research Letter*, **45**, 4180–4188, https://doi.org/10.1029/2018GL077408,

Meinen, C. S., Piola, A. R., Perez, R. C., & Garzoli, S. L. (2012). Deep Western Boundary Current transport variability in the South Atlantic: preliminary results from a pilot array at 34.5ºS, *Ocean Science*, **8**, 1041–1054, https://doi.org/10.5194/os-8-1041-2012.

Meinen, C. S., Garzoli, S. L., Perez, R. C., Campos, E., Piola, A. R., Chidichimo, M. P., et al. (2017). Characteristics and causes of Deep Western Boundary Current transport variability at 34.5ºS during 2009–2014, *Ocean Science*, **13**, 175-194, https://doi.org/10.5194/os-13-175-2017

Meredith, M. P., Woodworth, P. L., Chereskin, T. K., Marshall, D. P., Allison, L. C., Bigg, G. R., et al. (2011). Sustained monitoring of the Southern Ocean at Drake Passage: Past achievements and future priorities. *Reviews of Geophysics*, **49**, RG4005. https://doi.org/10.1029/2010RG000348

Orsi, A. H., Whitworth, T. III, & Nowlin, W. D. Jr. (1995). On the meridional extent and fronts of the Antarctic Circumpolar Current, *Deep-Sea Research Part I*, **42**, 641–673.

Renault, L., Molemaker, M. J., McWilliams, J. C., Shchepetkin, A. F., Lemarie, F., Chelton, D., et al. (2016). Modulation of wind work by oceanic current interaction with the atmosphere. *Journal of Physical Oceanography*, **46**, 1685–1704, https://doi.org/10.1175/JPO-D-15-0232.1

Richardson, P. L. (2007). Agulhas leakage into the Atlantic estimated with subsurface floats and surface drifters, *Deep-Sea Research Part I*, **54**, 1361 –1389.

Richardson, P. L. (2008). On the history of meridional overturning circulation schematic diagrams. *Progress in Oceanography*, **76**, pp. 466-486, https://doi.org/10.1016/j.pocean.2008.01.005

Rintoul, S. R. (1991). South Atlantic interbasin exchange, *Journal of Geophysical Research-Oceans*, **96**(C2), 2675–2692, https://doi.org/10.1029/90JC02422.

Rio, M.-H., Mulet, S., & Picot, N. (2014). Beyond GOCE for the ocean circulation estimate: Synergetic use of altimetry, gravimetry, and in situ data provides new insight into geostrophic and Ekman currents. *Geophysical Research Letter*, **41**, 8918–8925, https://doi.org/10.1002/2014GL061773.

Roemmich, D., Church, J., Gilson, J., Monselesan, D., Sutton, P., & Wijffels, S. (2015) Unabated planetary warming and its ocean structure since 2006. *Nature Climate Change*. **5**, 240-245, https://doi.org/10.1038/nclimate2514

Saunders, P. M., & King, B. A. (1995). Oceanic fluxes on the WOCE A11 section, *Journal of Physical Oceanography*, **25**, 1942–1958.

Schlitzer, R. (1996). Mass and Heat Transports in the South Atlantic Derived from Historical Hydrographie Data. In *The South Atlantic*. Springer, Berlin, Heidelberg

Schmitz, W. J. Jr., (1995). On the interbasin-scale thermohaline circulation, *Reviews of Geophysics*, **33**(2), 151–173, https://doi.org/10.1029/95RG00879.

Schmitz, W. J. Jr. (1996). On the World Ocean Circulation: Volume I. Technical Report, WHOI-96-03. 140 pp.

Speer, K. & Tziperman, E. (1992). Rates of water mass formation in the North Atlantic Ocean. *Journal of Physical Oceanography*, *22*(1), pp.93-104.

Speer, K. G., Siedler, G. & Talley, L. (1995). The Namib Col Current. *Deep-Sea Research Part I*, **42**, 1933–1950.

Speer, K. G. & Zenk, W. (1993). The flow of Antarctic Bottom Water into the Brazil Basin, *Journal of Physical Oceanography*, 23, 2667-2682.

Stramma, L., & England, M. (1999). On the water masses and mean circulation of the South Atlantic Ocean, *Journal of Geophysical Research*, **104**, 20,863–20,883, https://doi.org/10.1029/1999JC900139.

Swart, S., Speich, S., Ansorge, I. J., Goni, G. J., Gladyshev, S. & Lutjeharms J. R. E. (2008). Transport and variability of the Antarctic Circumpolar Current south of Africa, *Journal of Geophysical Research-Oceans*, **113**, C09014, https://doi.org/10.1029/2007JC004223

Talley, L. D. (2013). Closure of the Global Overturning Circulation Through the Indian, Pacific, and Southern Oceans: Schematics and Transports. *Oceanography*, **26** (1), 2013, pp. 80–97.

Valdivieso, M. Haines, K., Balmaseda, M., Chang, Y., Drevillon, M., Ferry, N., et al. (2017). An assessment of air–sea heat fluxes from ocean and coupled reanalyses. *Climate Dynamics*, **49** (3), 983-1008, https://doi.org/10.1007/s00382-015-2843-3

Walin, G. (1982). On the relation between sea-surface heat flow and thermal circulation in the ocean. *Tellus*, *34*(2), pp.187-195.

Warren, B. A. & Speer, K.G. (1991). Deep circulation in the eastern South Atlantic Ocean, *Deep-Sea Research Part A*, **38** (1991), pp. S281-S322

Whitworth, T., III (1983). Monitoring the transport of the Antarctic Circumpolar Current at Drake Passage, *Journal of Physical Oceanography*, **13**, 2045–2057.

Whitworth, T., III, & Peterson R. G. (1985). Volume transport of the Antarctic Circumpolar Current from bottom pressure measurements, *Journal of Physical Oceanography*, **15**, 810–816.

Whitworth, T., & Nowlin, W. D. (1987). Water masses and currents of the Southern Ocean at the Greenwich meridian, *Journal of Geophysical Research*, **92** (C6), 6462– 6476.

Wu, Z., & Huang, N. E. (2009). Ensemble empirical mode decomposition: A noise-assisted data analysis method, *Advances in Adaptive Data Analysis*, **1**(1), 1–41, https://doi.org/10.1142/S1793536909000047

Xu, X., Schmitz, W. J. Jr., Hurlburt, H. E., & Hogan, P. J. (2012). Mean Atlantic meridional overturning circulation across 26.5N from eddy resolving simulations compared to observations. *Journal of Geophysical Research-Oceans*, **117**, C03042, https://doi.org/10.1029/2010JC007586.

Xu, X., Chassignet, E. P., Johns, W. E., Schmitz W. J. Jr., & Metzger, E. J. (2014). Intraseasonal to interannual variability of the Atlantic meridional overturning circulation from eddy-resolving simulations and observations. *Journal of Geophysical Research-Oceans*, **119**, 5140–5159, https://doi.org/10.1002/2014JC009994.

Xu, X., P. B. Rhines, & E. P. Chassignet, 2018, On mapping the diapycnal water mass transformation of the upper North Atlantic Ocean, Journal of Physical Oceanography, 48, 2233-2258, doi:10.1175/JPO-D-17-0223.1.

Xu, X., E. P. Chassignet and F. Wang, 2018b, On the variability of the Atlantic meridional overturning circulation transports in coupled CMIP5 simulations, Climate Dynamics, doi:10.1007/s00382-018-4529-0

Yu, L., Jin, X., & Weller, R. A. (2008) Multidecade Global Flux Datasets from the Objectively Analyzed Air-sea Fluxes (OAFlux) Project: Latent and sensible heat fluxes, ocean evaporation, and related surface meteorological variables. Woods Hole Oceanographic Institution, OAFlux Project Technical Report. OA-2008-01, 64pp. Woods Hole. Massachusetts.

Zhang, R. (2010). Latitudinal dependence of Atlantic meridional overturning circulation (AMOC) variations, *Geophysical Research Letter*, **37**, L16703, https://doi.org/10.1029/2010GL044474

Zweng, M. M, Reagan, J. R., Antonov, J. I., Locarnini, R. A., Mishonov, A.V., Boyer, T.P., et al. (2013). Salinity. Vol. 2, World Ocean Atlas 2013, S. Levitus, Ed., A. Mishonov Technical Ed.; NOAA Atlas NESDIS 74, 39 pp.

Figure Captions:

Figure 1: Model bathymetry (in km) along with key topographic features in the South Atlantic Ocean. Red lines denote three sections where significant observations have been obtained and the observations are used to evaluate the model results: 34°S in the South Atlantic, 65°W in the Drake Passage, and the Prime Meridian-Good Hope (PM-GH) transect southwest of Africa.

Figure 2: Time evolution of global domain-averaged a) potential temperature in °C and b) total kinetic energy in cm^2s^{-2} from the global ocean-sea ice simulation. Thin and thick lines denote monthly and annual means, respectively.

Figure 3: Time evolution of a) monthly mean sea ice extent and b) annual mean sea ice extent anomaly relative to the 1980-2015 average. The sea ice extent is defined as the area (in 10^6 km^2) with sea ice concentration of 15% or higher. The red/blue lines are model results in the northern/southern hemisphere; black lines are observations from NSIDC (National Snow and Ice Data Center).

Figure 4: a) Time evolution of the modeled monthly mean transport of the Atlantic meridional overturning circulation (AMOC) at 26.5°N; blue dash line denotes a decreasing trend of 0.43 Sv per decade; b) Variability of the AMOC transports during 2004-2015, with thin/thick lines denoting monthly/annual means; c) Seasonal variability of the AMOC transports at 26.5°N averaged over 2004-2015. Red/black in panels b-c) are model results and observations from the RAPID array.

Figure 5: Observed and modeled distributions of a-b) time mean sea surface height (SSH, in cm), c-d) SSH standard deviation (in cm), and e-f) eddy kinetic energy (EKE, in cm^2 s^{-2}) of the surface current in the southern Atlantic. In observation, the mean SSH is based on long-term climatology CNES-CLS13 (Rio et al., 2014); the SSH standard deviation and EKE are based on AVISO data in 1993-2012. All model results are in 1993-2012.

Figure 6: Observed (upper panel) and modeled (lower panel) sea-surface height (SSH) anomaly along the Prime Meridian in latitude range 20-40_S from 2003 to 2012. The black `+' denotes the latitude of the Agulhas Rings that pass this longitude.

Figure 7: Observed and modeled potential temperature and salinity across 34°S. Observations are based on a combination of Argo pro_les (2004-2014) for the top 2000m and World Ocean Atlas 2013 (WOA13) below 2000 m; model results based on the global 1/12° HYCOM simulation in 1981-2015; The three black lines denote isopycnic interfaces that divide the water column into four layers: near surface water ($\sigma_2 < 35.65$ kg m^{-3}), Antarctic Intermediate Water (AAIW, $35.65 < \sigma_2 < 36.58$), North Atlantic Deep Water (NADW, $36.58 < \sigma_2 < 37.12$), and Antarctic Bottom Water (AABW, $\sigma_2 > 37.12$).

Figure 8: Observed and modeled time mean meridional velocity across 34°S and the corresponding volume transport for the four density layers: surface water ($\sigma_2 < 35.65$ kg m^{-3}), Antarctic Intermediate Water (AAIW, $35.65 < \sigma_2 < 36.58$), North Atlantic Deep Water (NADW, $36.58 < \sigma_2 < 37.12$), and Antarctic Bottom Water (AABW, $\sigma_2 > 37.12$). Observations based on a combination of Argo-WOA13 profiles; model results based on global 1/12° HYCOM simulation in 1981-2015.

Figure 9: a) Long-term mean meridional overturning streamfunction (in Sv) at 34°S with respect to a) depth and b) potential density in σ_2. Observations based on monthly mean Argo profile for the upper 2000m and WOA13 below 2000 m; model results based a global 1/12° HYCOM simulation (1981-2015).

Figure 10: a) Time series of the observed (black) and modeled (red) AMOC transport at 34°S, with thin/ thick lines denoting monthly/annual means, respectively; b) seasonal variability of the AMOC transports at 34°S, averaged over 2004-2014 in observations (black) and 1981-2015 in model results(red).

Figure 11: Modeled long-term mean zonal velocity and the corresponding four-layer volume transport in four density layers across a) 65°W in the Drake Passage and b) the Prime Meridian-Good Hope (PM-GH) transect southwest of Africa. The ∇ denote the locations of Antarctic circumpolar current (ACC) fronts, from south to north, the Southern Boundary, South ACC Front, Polar Front, Subantarctic Front, as well as the subtropical front (only in panel b). The shaded area in panel b) between 40 and 55.5°S marks the ACC regime across the PM-GH transect. Transport are accumulative northward. The four layers are near surface water ($\sigma_2 < 35.65$ kg m^{-3}), Antarctic Intermediate Water (AAIW, $35.65 < \sigma_2 < 36.58$), North Atlantic Deep Water (NADW, $36.58 < \sigma_2 < 37.12$), and Antarctic Bottom Water (AABW, $\sigma_2 > 37.12$).

Figure 12: a) Modeled mean horizontal transports (in Sv) for very 100 m in the vertical across the 34°S, the 65°W, and the PM-GH transects. b) The net transports into the region enclosed by the three transects, with positive (negative) values indicating net transport into (out of) the region.

Figure 13: a) Variability of the modeled ACC transport through the Drake Passage at the 65°W, in monthly (thin) and annual (thick) means; b) Seasonal variability of the modeled ACC transports averaged over 1981-2015.

Figure 14: a) Net transports into the South Atlantic region closed by the 34°S, the 65°W, and the PM-GH transects, with respect to density layers (positive/negative values for net transport into/out of the region); b) Black line denotes the total diapycnal transformation; and dashed red line denotes the surface forced diapycnal transformation calculated from surface buoyancy fluxes.

Figure 15: Modeled long-term mean horizontal transport streamfunction (in Sv) for the layer of near surface water ($\sigma_2 < 35.65$ kg m^{-3}). Each streamline contour is 2 Sv. Red, blue, and orange streamlines denote AMOC contribution, super gyre that ow around the South Atlantic and back to Indian Ocean, and subtropical gyre of the South Atlantic.

Figure 16: Modeled long-term mean horizontal transport streamfunction (Sv) for the layer of AAIW ($35.65 < \sigma_2 < 36.58$ kg m^{-3}). Thick pink stream lines (increment of 8 Sv) is the ACC. The Red, blue, and orange streamlines denote AMOC contribution, super gyre, and subtropical gyre of the South Atlantic (similar to Figure 15). The dashed blue lines denote 34°S, 45°S, and the GoodHope sections, across which the water properties of the northward and northwestward transports are examined Figure 17.

Figure 17: Modeled northward transport (in Sv) across 45°S and 34°S, and northwestward transport across the GH section, projected on potential temperature-salinity (θ-S) plane with $\Delta\theta \times \Delta S$ of 0.2°C×0.04. The isopycnal (σ_2) surfaces of 35.65 and 36.58 kg m^{-3} denote the upper and lower AAIW interfaces.

Figure 18: Modeled long-term mean horizontal transport streamfunction for the layer of NADW ($36.58 < \sigma_2 < 37.12$ kg m^{-3}). Pink streamlines (10 Sv increment) indicate the eastward transport of the ACC, blue to yellow streamlines (2 Sv increment) represent the southward spreading of the NADW from north.

Figure 19: a) observed and model salinity distribution at 2500m in the South Atlantic. Observation based on CTD data from GoShip program http://www.go-ship.org. Detailed vertical sections can be seen in the WOCE Atlas (Kiltermann et al., 2011). The results show an eastward extension of high salinity (NADW signature) between 20 and 25°S west of the mid-Atlantic Ridge (MAR), and significantly lower salinity east of MAR.

Figure 20: Zoomed view of the circulation for the density layer of NADW ($36.58 < \sigma_2 < 37.12$ kgm^{-3}) across the Mid-Atlantic Ridge in the South Atlantic Ocean. The blue contours denote NADW from north and magenta streamlines denote ACC from Drake Passage.

Figure 21: Modeled seasonal variability of the AMOC transports at different latitude, based on the third Intrinsic mode function (IMF) using the ensemble empirical mode decomposition (EEMD, Huang and Wu (2008) and Wu and Huang (2009).

Figure 22: Modeled interannual variability of the AMOC transports at different latitude, based on the fourth and fifth Intrinsic mode function (IMF) using the ensemble empirical mode decomposition (EEMD, Huang and Wu (2008) and Wu and Huang (2009).

Figure 23: Modeled decadal variability of the AMOC transports at different latitude, based on the sixth and seventh Intrinsic mode function (IMF) using the ensemble empirical mode decomposition (EEMD, Huang and Wu (2008) and Wu and Huang (2009).

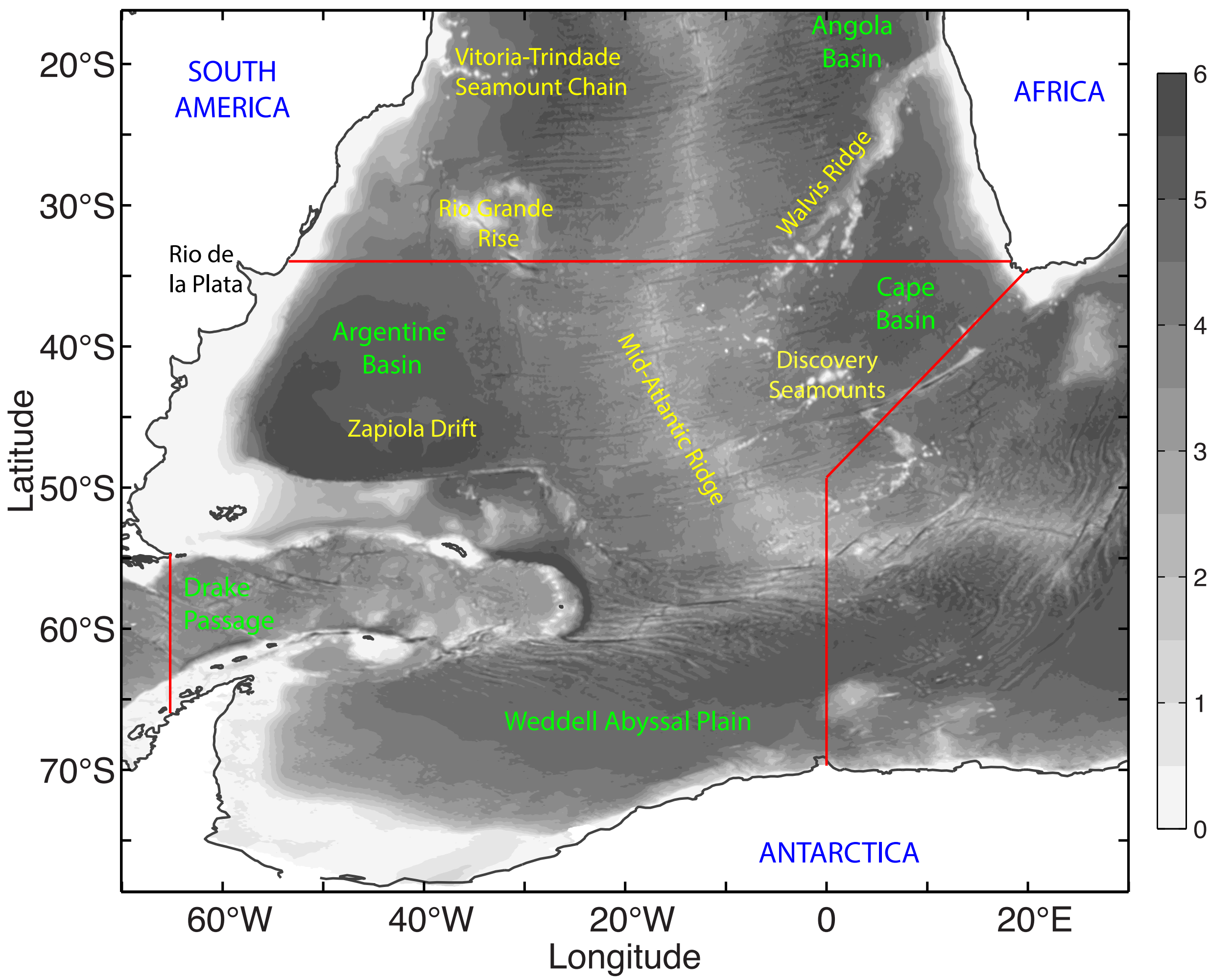

Figure 1: Model bathymetry (in km) along with key topographic features in the South Atlantic Ocean. Red lines denote three sections where significant observations have been obtained and the observations are used to evaluate the model results: 34°S in the South Atlantic, 65°W in the Drake Passage, and the Prime Meridian-Good Hope (PM-GH) transect southwest of Africa.

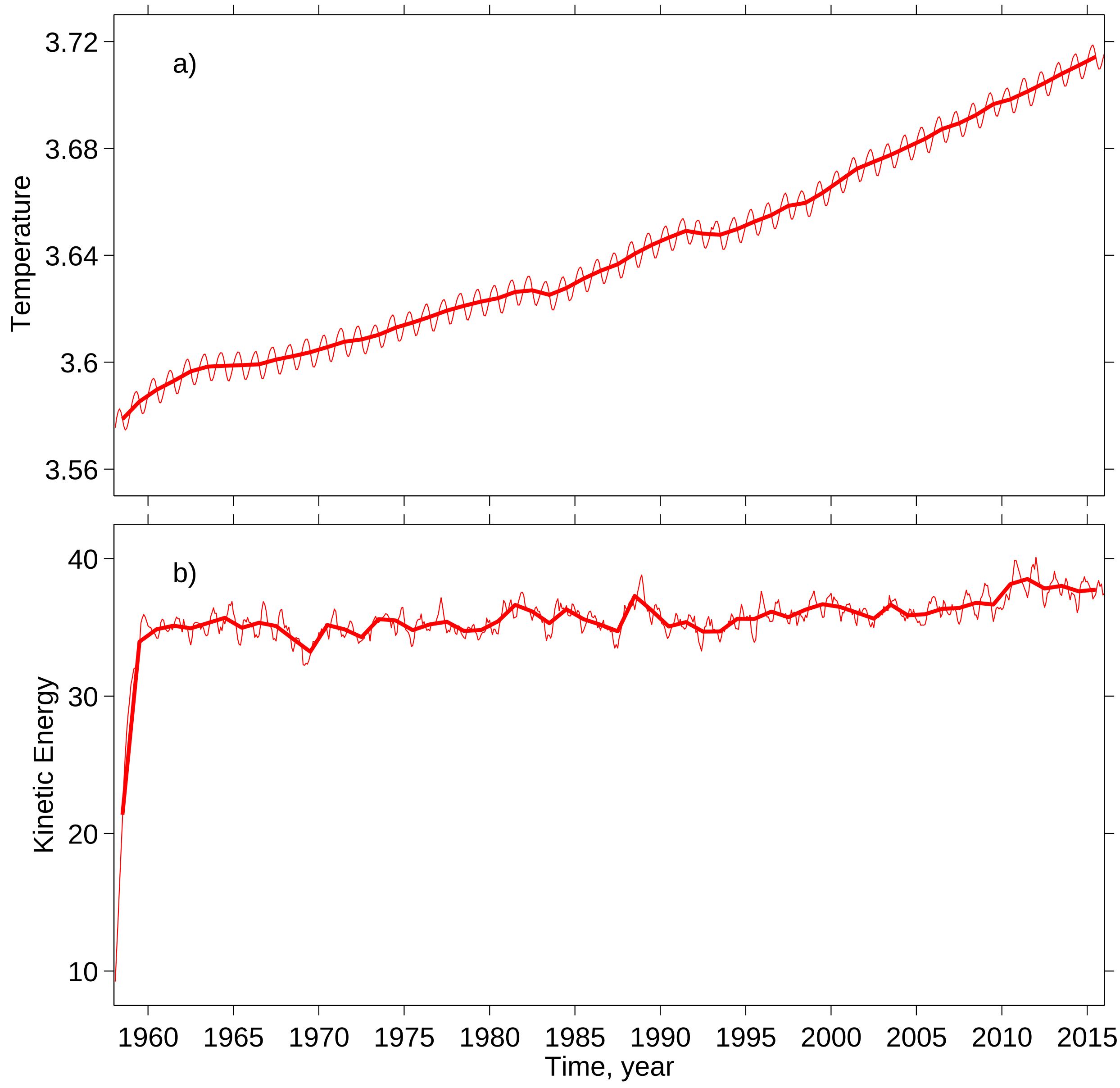

Figure 2: Time evolution of global domain-averaged a) potential temperature in °C and b) total kinetic energy in $cm^2 s^{-2}$ from the global ocean-sea ice simulation. Thin and thick lines denote monthly and annual means, respectively.

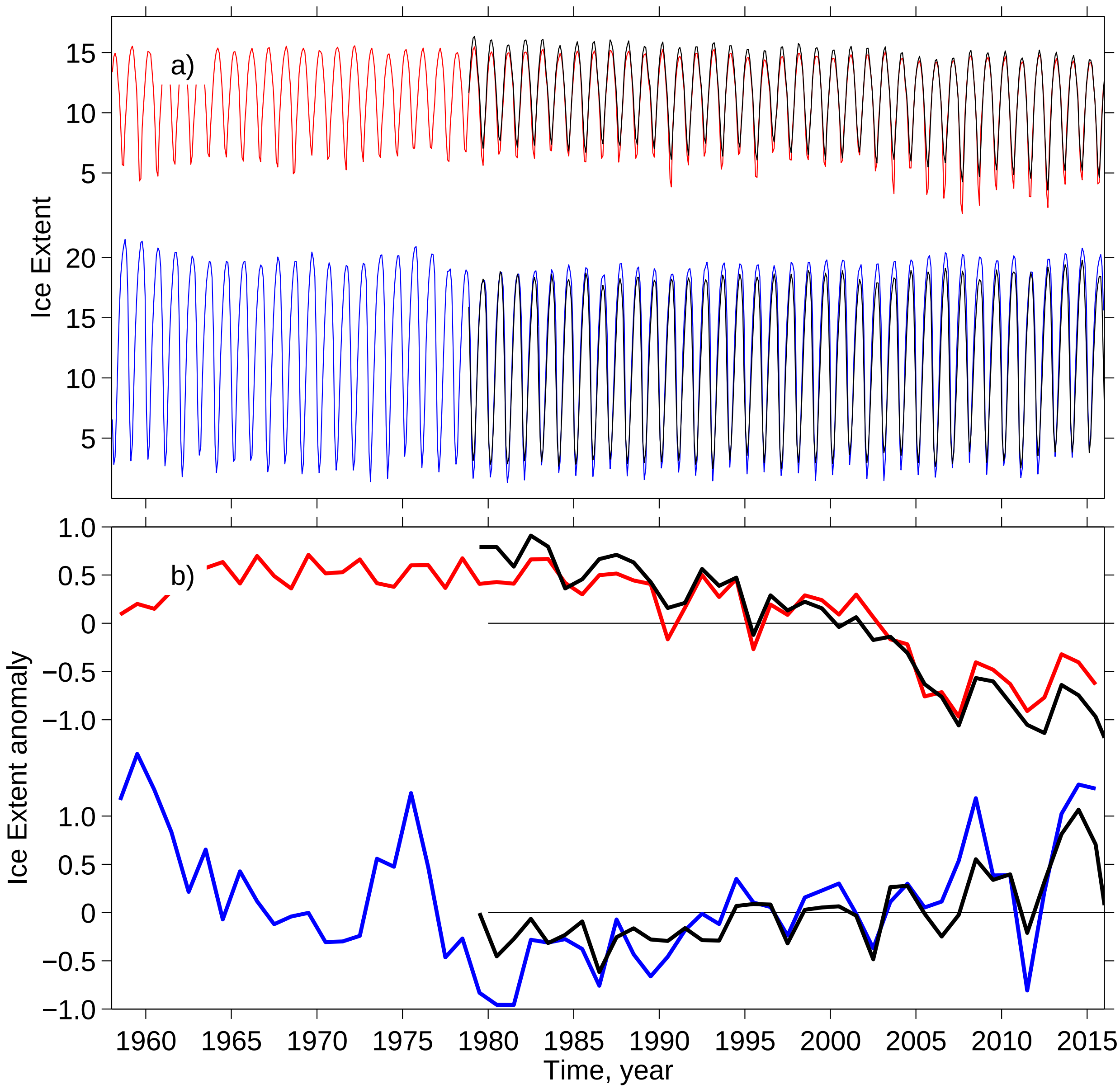

Figure 3: Time evolution of a) monthly mean sea ice extent and b) annual mean sea ice extent anomaly relative to the 1980-2015 average. The sea ice extent is defined as the area (in 10^6 km^2) with sea ice concentration of 15% or higher. The red/blue lines are model results in the northern/southern hemisphere; black lines are observations from NSIDC (National Snow and Ice Data Center).

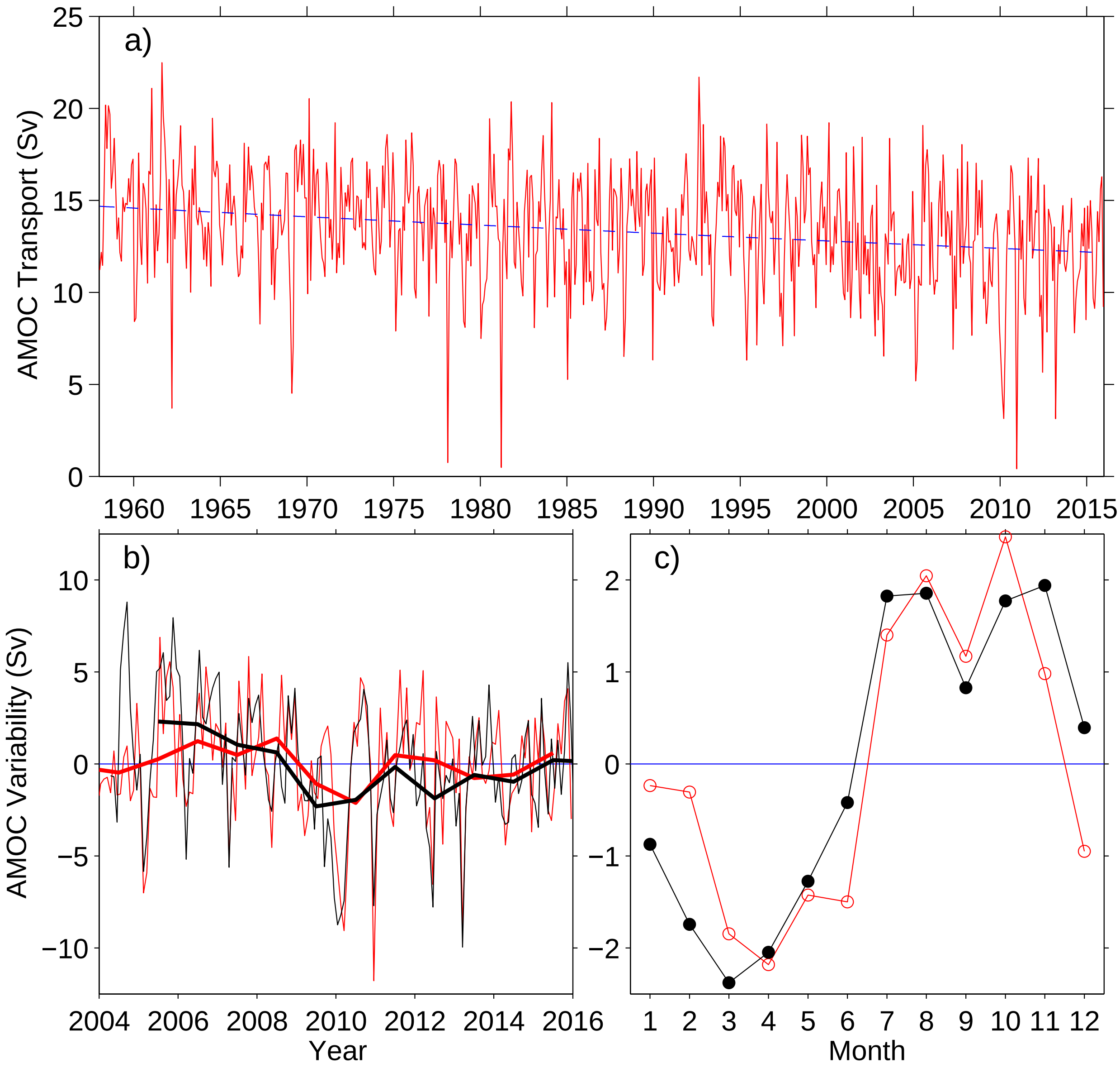

Figure 4: a) Time evolution of the modeled monthly mean transport of the Atlantic meridional overturning circulation (AMOC) at 26.5°N; blue dash line denotes a decreasing trend of 0.43 Sv per decade; b) Variability of the AMOC transports during 2004-2015, with thin/thick lines denoting monthly/annual means; c) Seasonal variability of the AMOC transports at 26.56∘N averaged over 2004-2015. Red/black in panels b-c) are model results and observations from the RAPID array.

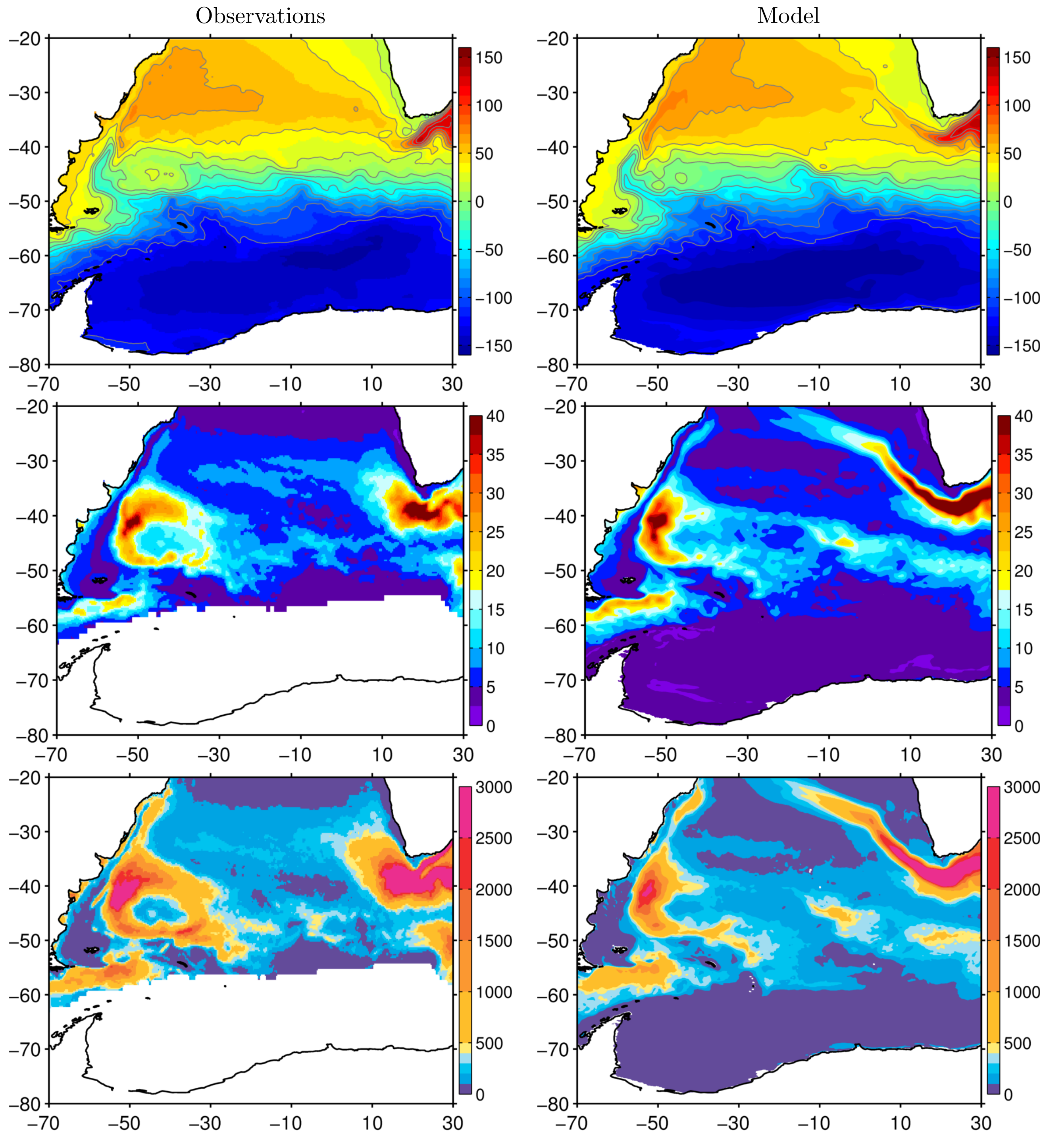

Figure 5: Observed and modeled distributions of a-b) time mean sea surface height (SSH, in cm), c-d) SSH standard deviation (in cm), and e-f) eddy kinetic energy (EKE, in $cm^2\,s^{-2}$) of the surface current in the southern Atlantic. In observation, the mean SSH is based on long-term climatology CNES-CLS13 (Rio et al., 2014); the SSH standard deviation and EKE are based on AVISO data in 1993-2012. All model results are in 1993-2012.

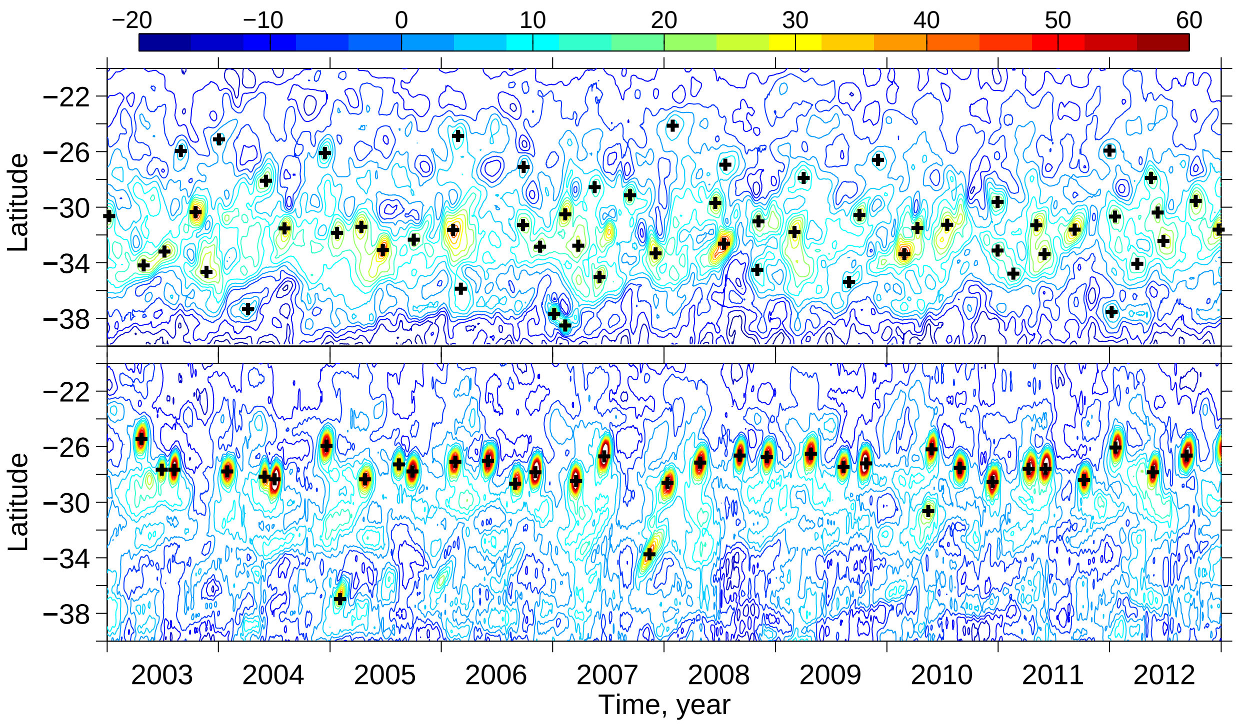

Figure 6: Observed (upper panel) and modeled (lower panel) sea-surface height (SSH) anomaly along the Prime Meridian in latitude range 20-40°S from 2003 to 2012. The black '+' denotes the latitude of the Agulhas Rings that pass this longitude.

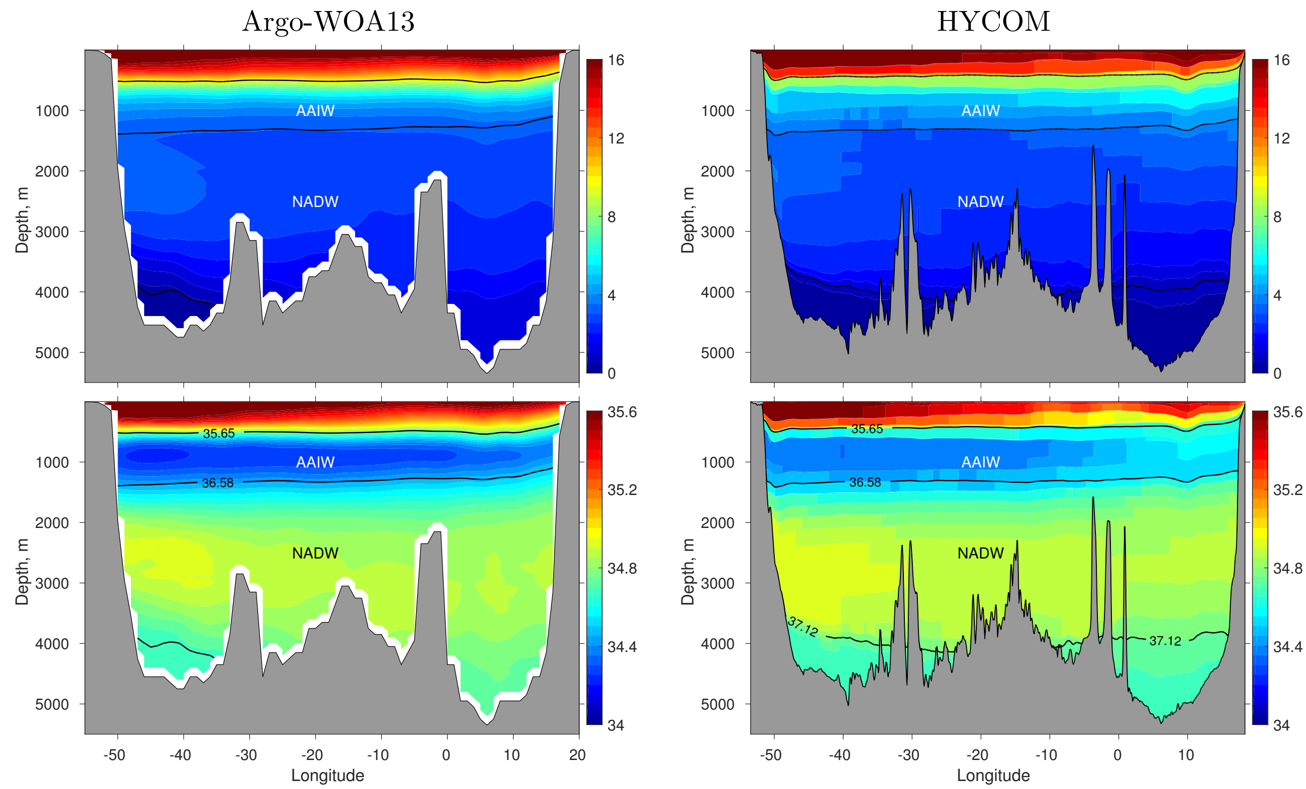

Figure 7: Observed and modeled potential temperature and salinity across 34°S. Observations are based on a combination of Argo profiles (2004-2014) for the top 2000 m and World Ocean Atlas 2013 (WOA13) below 2000 m; model results based on the global 1/12° HYCOM simulation in 1981-2015; The three black lines denote isopycnic interfaces that divide the water column into four layers: near surface water ($\sigma_2 < 35.65\,\mathrm{kg\,m^{-3}}$), Antarctic Intermediate Water (AAIW, $35.65 < \sigma_2 < 36.58$), North Atlantic Deep Water (NADW, $36.58 < \sigma_2 < 37.12$), and Antarctic Bottom Water (AABW, $\sigma_2 > 37.12$).

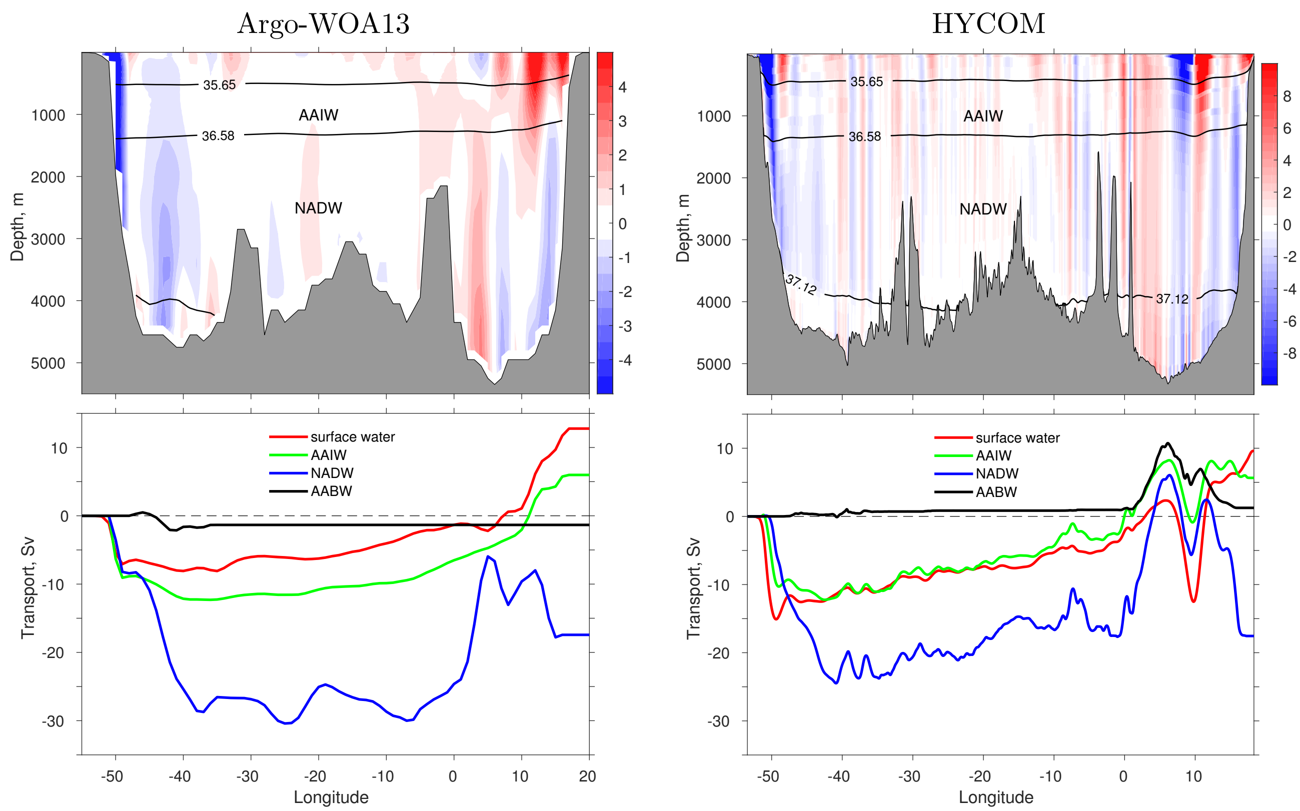

Figure 8: Observed and modeled time mean meridional velocity across 34°S and the corresponding volume transport for the four density layers: near surface water ($\sigma_2 < 35.65\,\mathrm{kg\,m^{-3}}$), Antarctic Intermediate Water (AAIW, $35.65 < \sigma_2 < 36.58$), North Atlantic Deep Water (NADW, $36.58 < \sigma_2 < 37.12$), and Antarctic Bottom Water (AABW, $\sigma_2 > 37.12$). Observations based on a combination of Argo-WOA13 profiles; model results based on global 1/12° HYCOM simulation in 1981-2015.

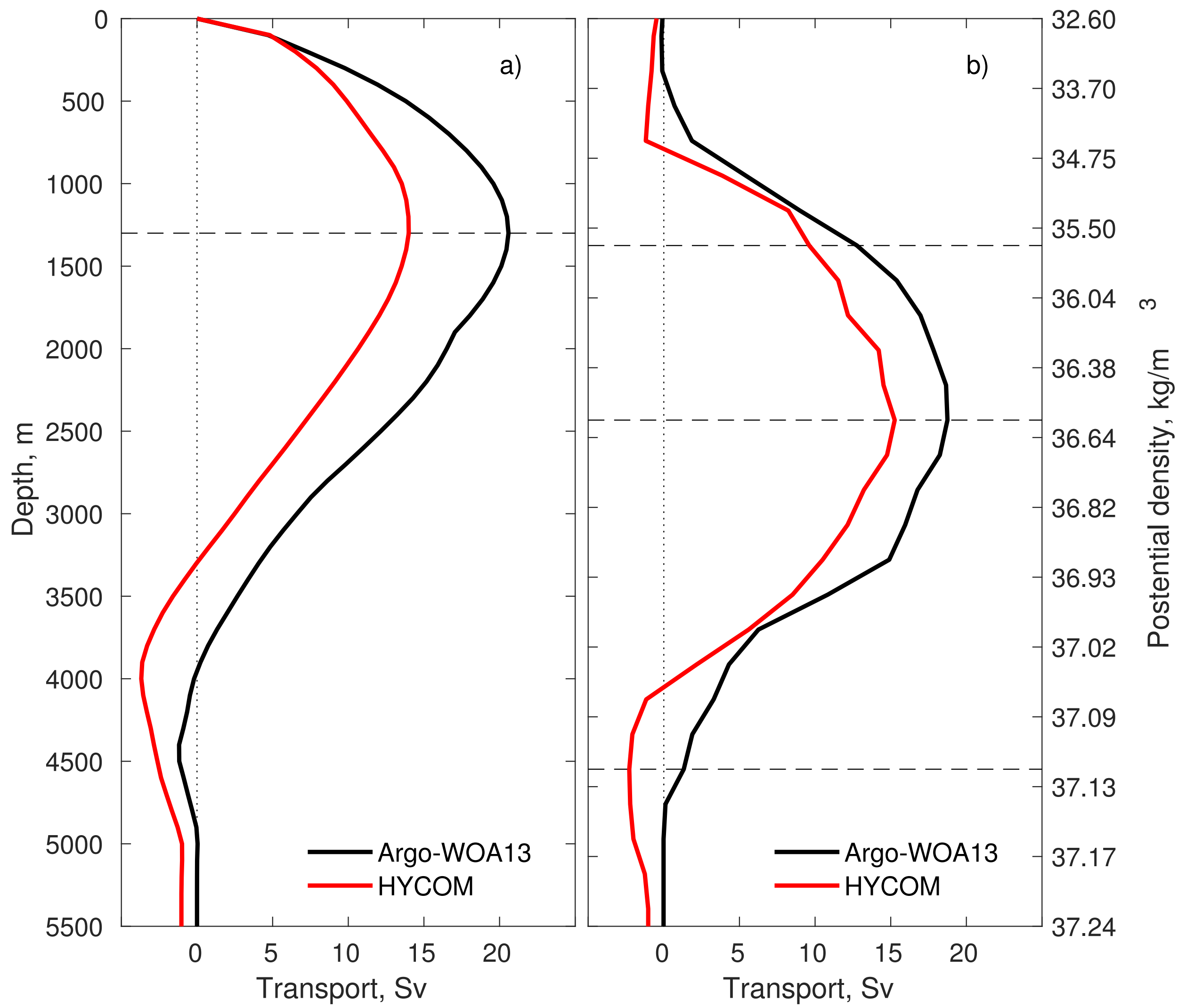

Figure 9: a) Long-term mean meridional overturning streamfunction (in Sv) at 34°S with respect to a) depth and b) potential density in σ_2. Observations based on monthly mean Argo profile for the upper 2000 m and WOA13 below 2000 m; model results based a global 1/12° HYCOM simulation (1981-2015).

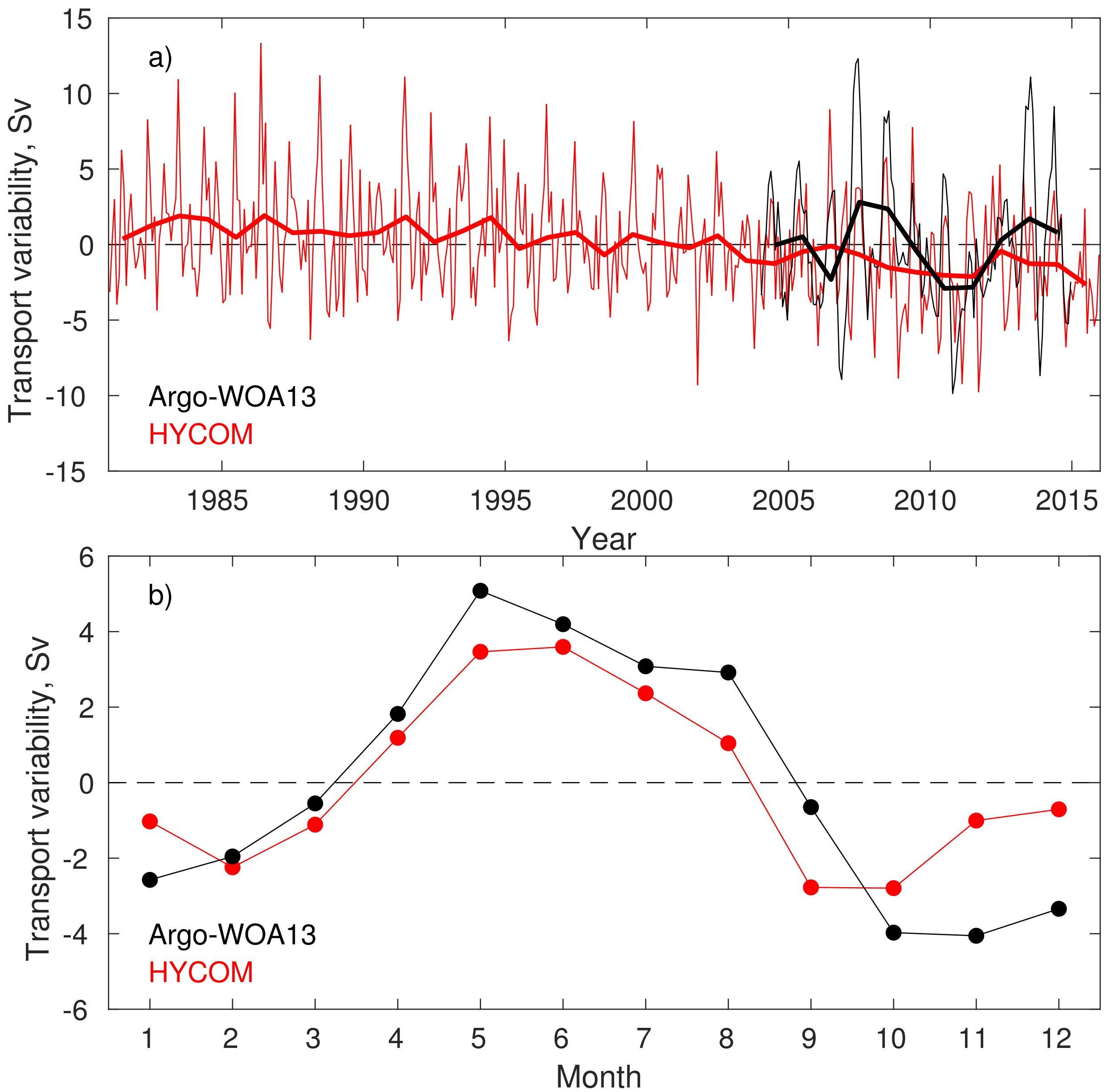

Figure 10: a) Time series of the observed (black) and modeled (red) AMOC transport at 34°S, with thin/thick lines denoting monthly/annual means, respectively; b) seasonal variability of the AMOC transports at 34°S, averaged over 2004-2014 in observations (black) and 1981-2015 in model results (red).

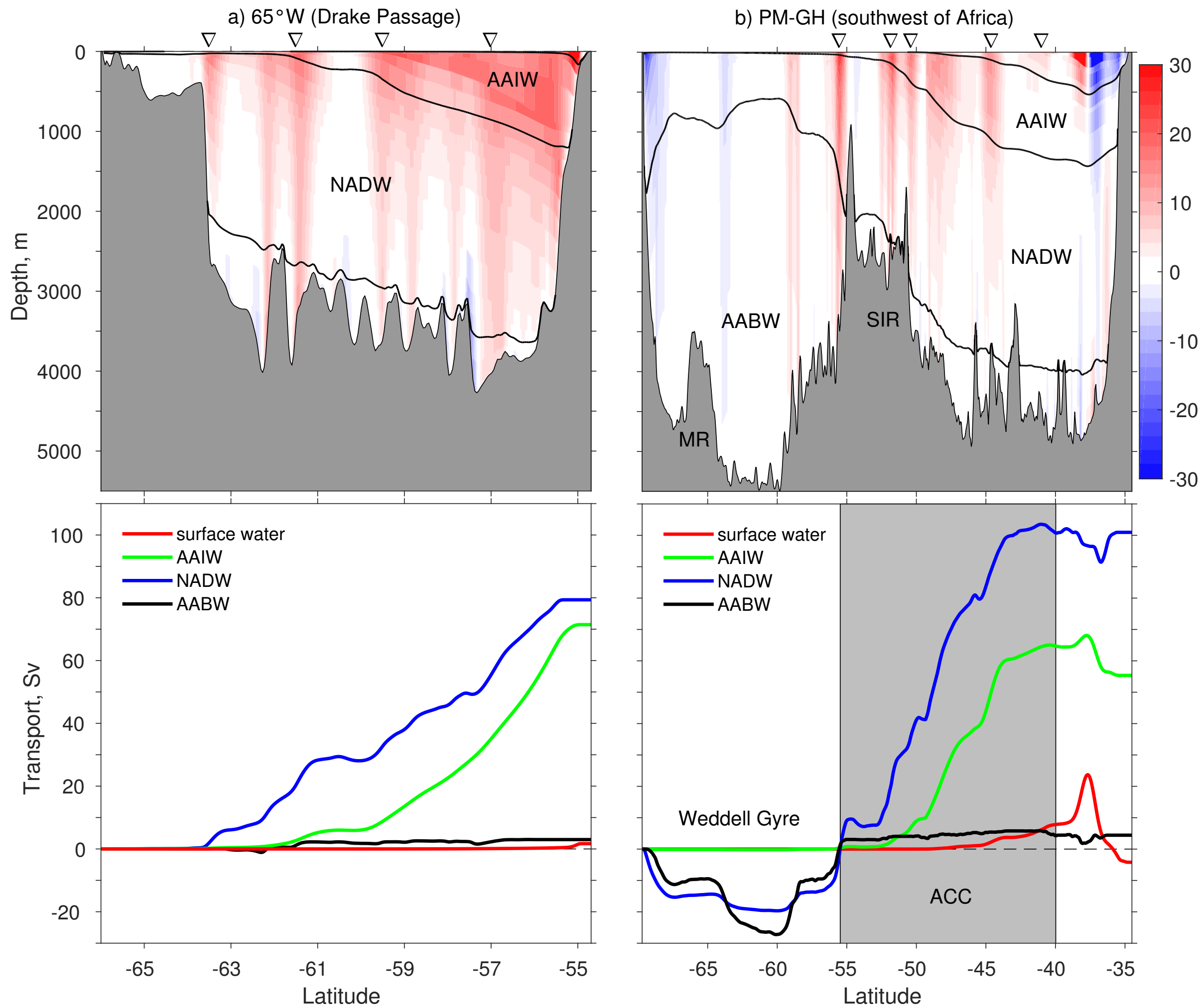

Figure 11: Modeled long-term mean zonal velocity and the corresponding four-layer volume transport in four density layers across a) 65°W in the Drake Passage and b) the Prime Meridian-Good Hope (PM-GH) transect southwest of Africa. The ∇ denote the locations of Antarctic circumpolar current (ACC) fronts, from south to north, the Southern Boundary, South ACC Front, Polar Front, Subantarctic Front, as well as the subtropical front (only in panel b). The shaded area in panel b) between 40 and 55.5°S marks the ACC regime across the PM-GH transect. Transport are accumulative northward. The four layers are near surface water ($\sigma_2 < 35.65\,\mathrm{kg\,m^{-3}}$), Antarctic Intermediate Water (AAIW, $35.65 < \sigma_2 < 36.58$), North Atlantic Deep Water (NADW, $36.58 < \sigma_2 < 37.12$), and Antarctic Bottom Water (AABW, $\sigma_2 > 37.12$).

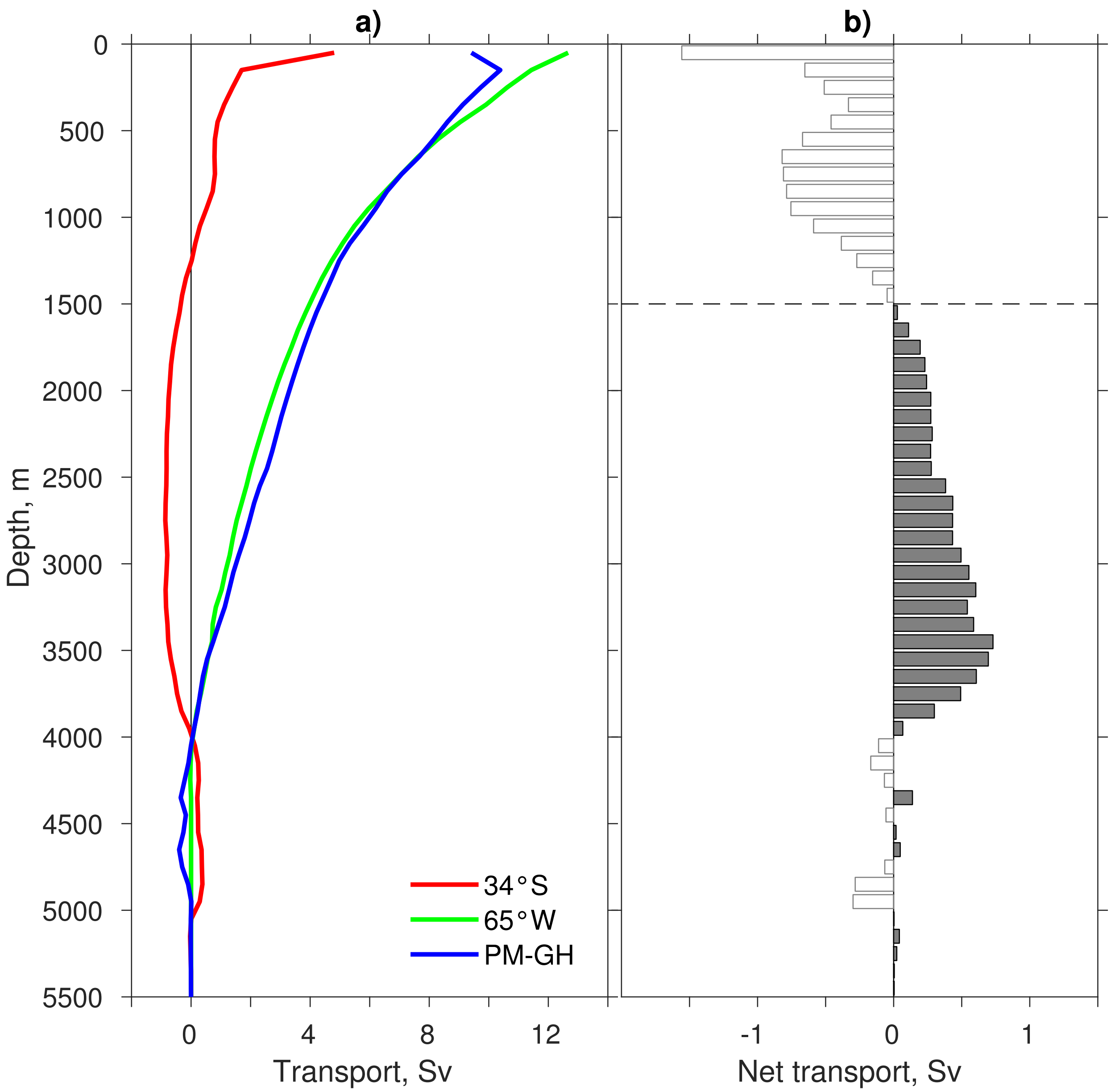

Figure 12: a) Modeled mean horizontal transports (in Sv) for very 100 m in the vertical across the 34°S, the 65°W, and the PM-GH transects. b) The net transports into the region enclosed by the three transects, with positive (negative) values indicating net transport into (out of) the region.

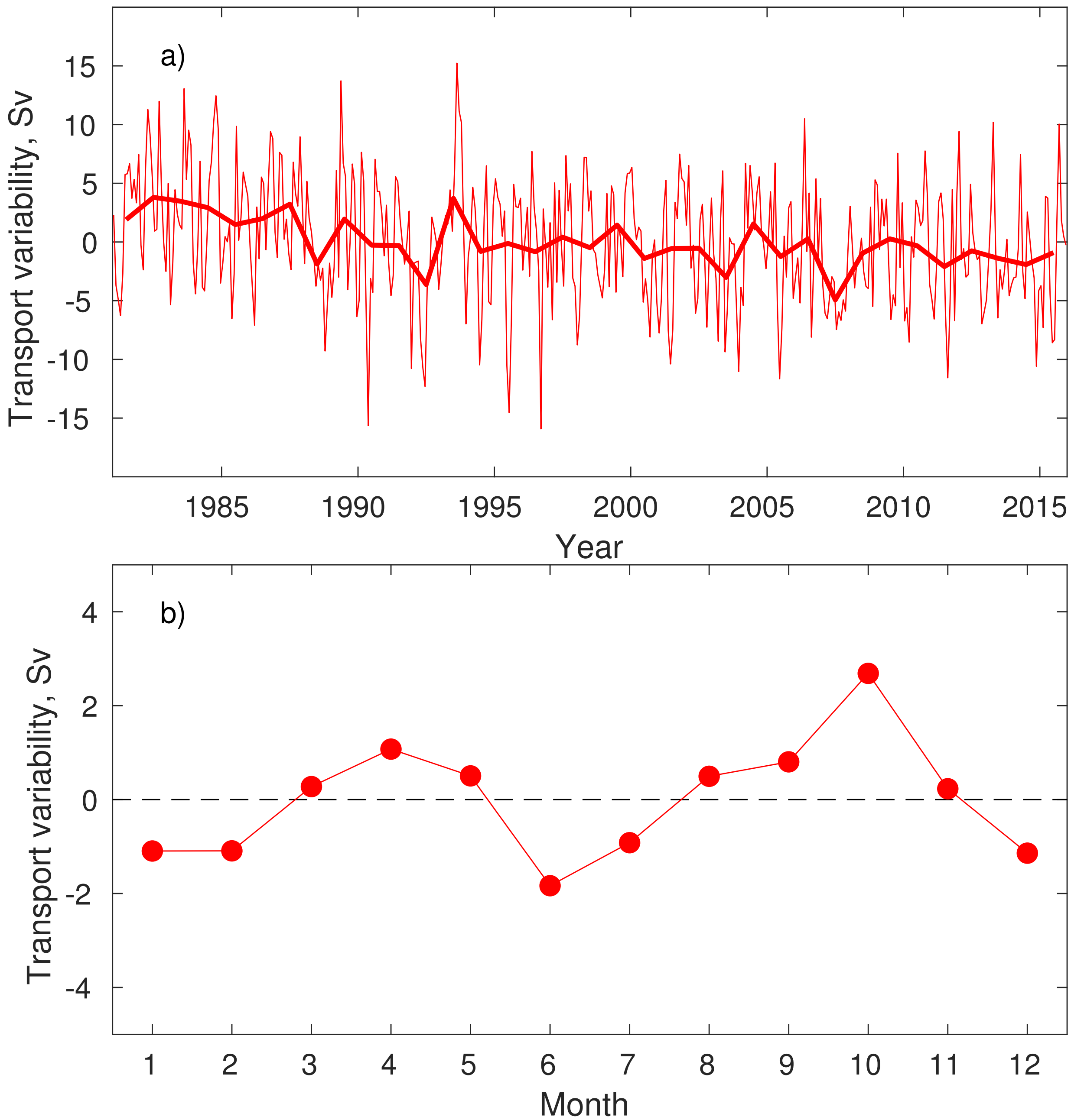

Figure 13: a) Variability of the modeled ACC transport through the Drake Passage at the 65°W, in monthly (thin) and annual (thick) means; b) Seasonal variability of the modeled ACC transports averaged over 1981-2015.

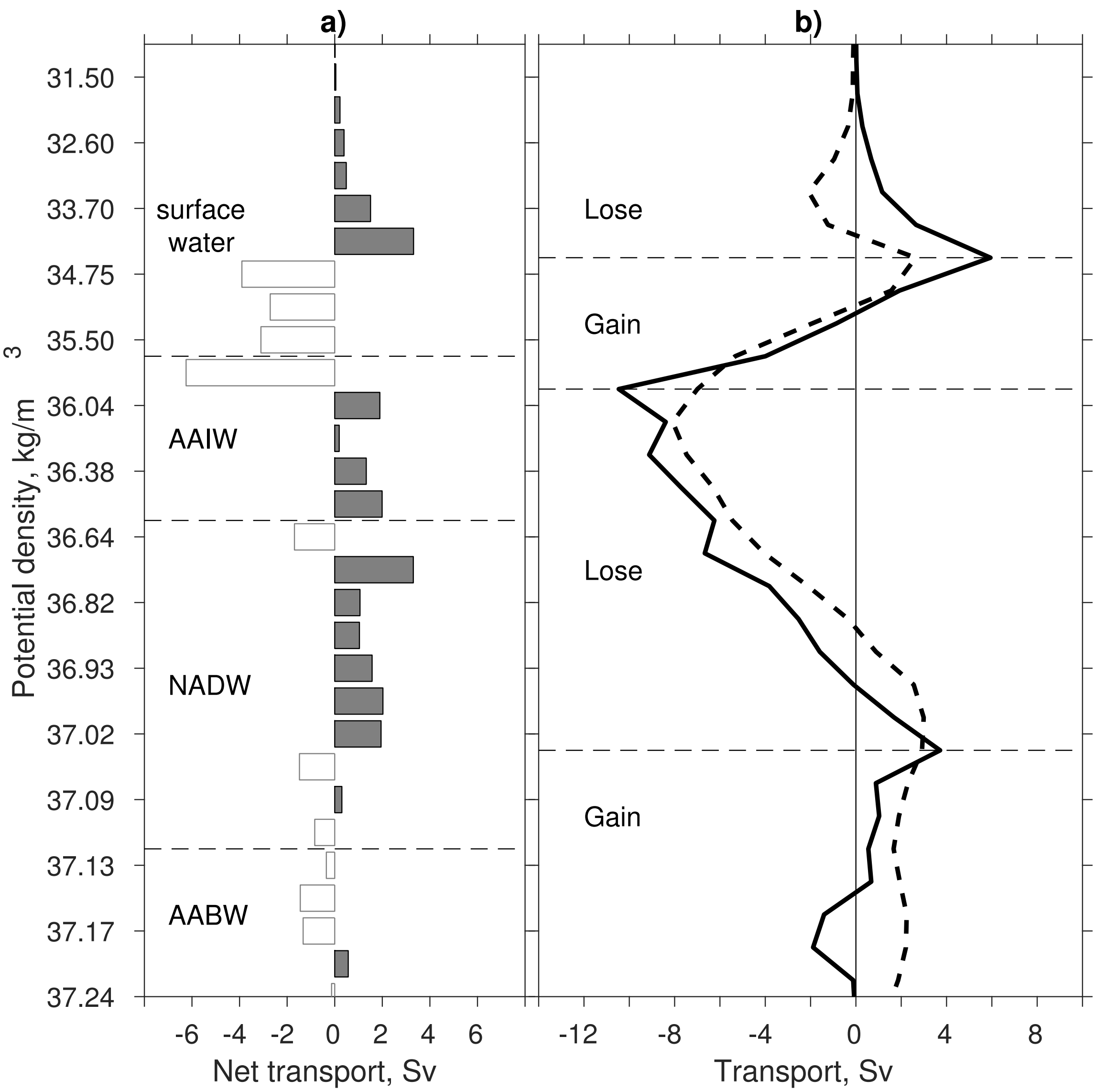

Figure 14: a) Net transports into the South Atlantic region closed by the 34°S, the 65°W, and the PM-GH transects, with respect to density layers (positive/negative values for net transport into/out of the region); b) Black line denotes the total diapycnal transformation; and dashed red line denotes the surface forced diapycnal transformation calculated from surface buoyancy fluxes.

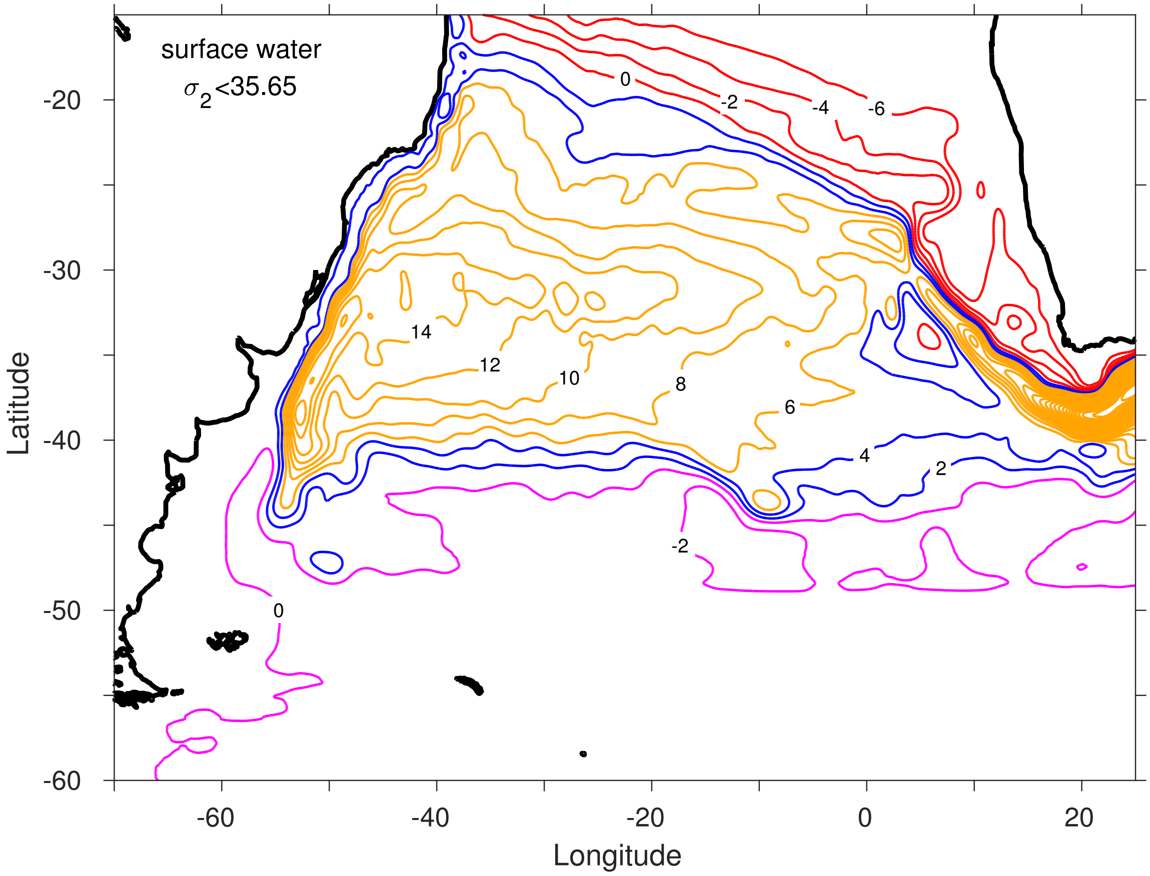

Figure 15: Modeled long-term mean horizontal transport streamfunction (in Sv) for the layer of near surface water ($\sigma < 35.65\,\mathrm{kg\,m^{-3}}$). Each streamline contour is $2\,\mathrm{Sv}$. Red, blue, and orange streamlines denote AMOC contribution, super gyre that flow around the South Atlantic and back to Indian Ocean, and subtropical gyre of the South Atlantic.

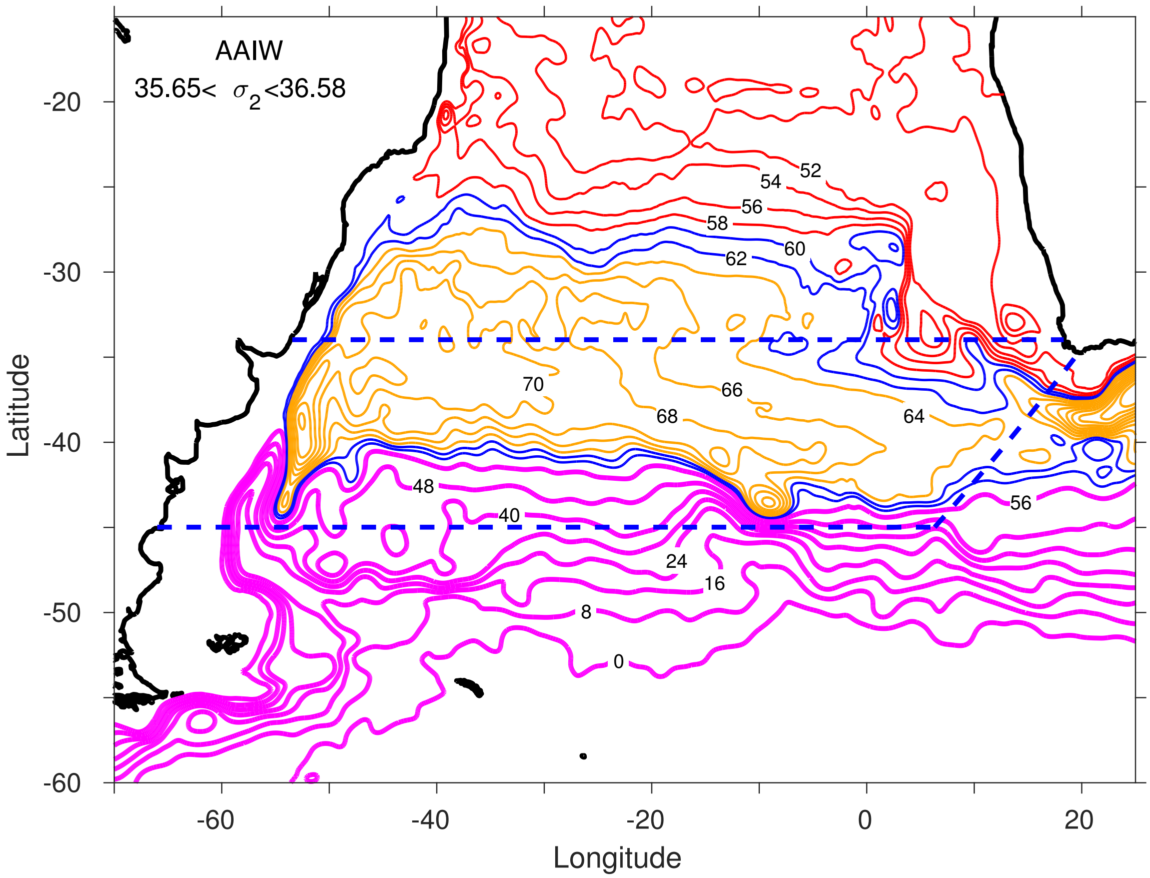

Figure 16: Modeled long-term mean horizontal transport streamfunction (Sv) for the layer of AAIW ($35.65 < \sigma < 36.58\,\mathrm{kg\,m^{-3}}$). Thick pink stream lines (increment of 8 Sv) is the ACC. The Red, blue, and orange streamlines denote AMOC contribution, super gyre, and subtropical gyre of the South Atlantic (similar to Figure 15). The dashed blue lines denote 34°S, 45°S, and the GoodHope sections, across which the water properties of the northward and northwestward transports are examined Figure 17.

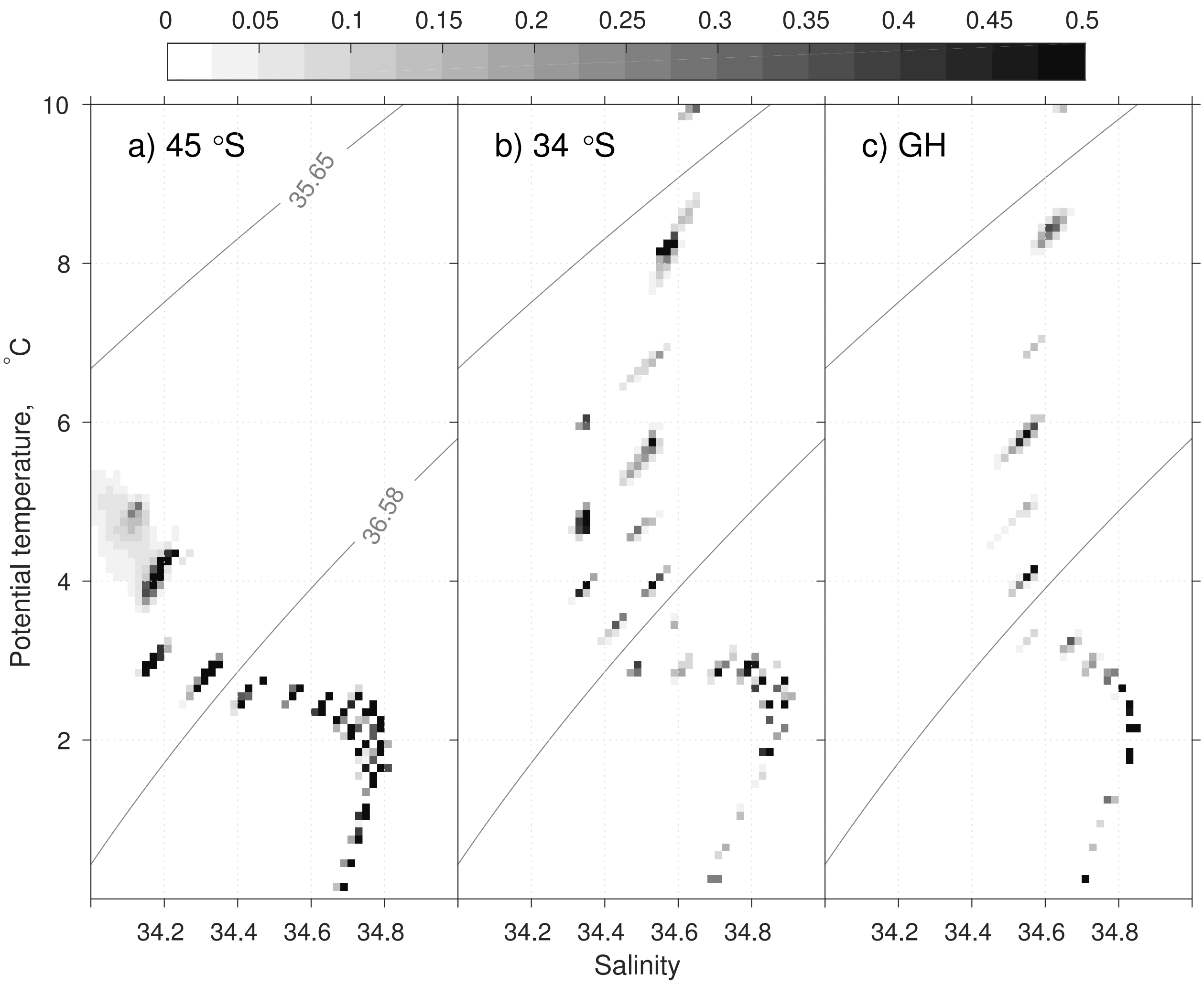

Figure 17: Modeled northward transport (in Sv) across 45°S and 34°S, and northwestward transport across the GH section, projected on potential temperature-salinity (θ-S) plane with $\Delta\theta \times \Delta \mathrm{S}$ of $0.2°\mathrm{C} \times 0.04$. The isopycnal ($\sigma_2$) surfaces of 35.65 and $36.58\,\mathrm{kg\,m^{-3}}$ denote the upper and lower AAIW interfaces.

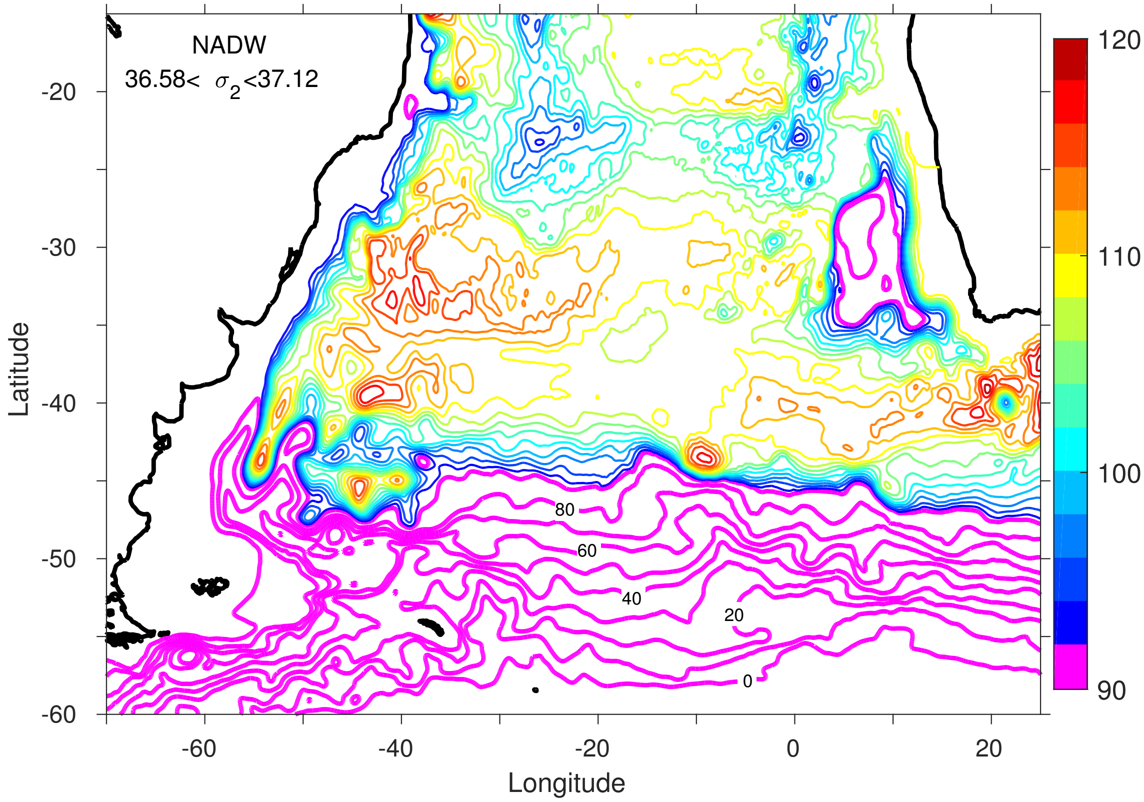

Figure 18: Modeled long-term mean horizontal transport streamfunction for the layer of NADW ($36.58 \leq \sigma_2 < 37.12\,\mathrm{kg\,m^{-3}}$). Pink streamlines (10 Sv increment) indicate the eastward transport of the ACC, blue to yellow streamlines (2 Sv increment) represent the southward spreading of the NADW from north.

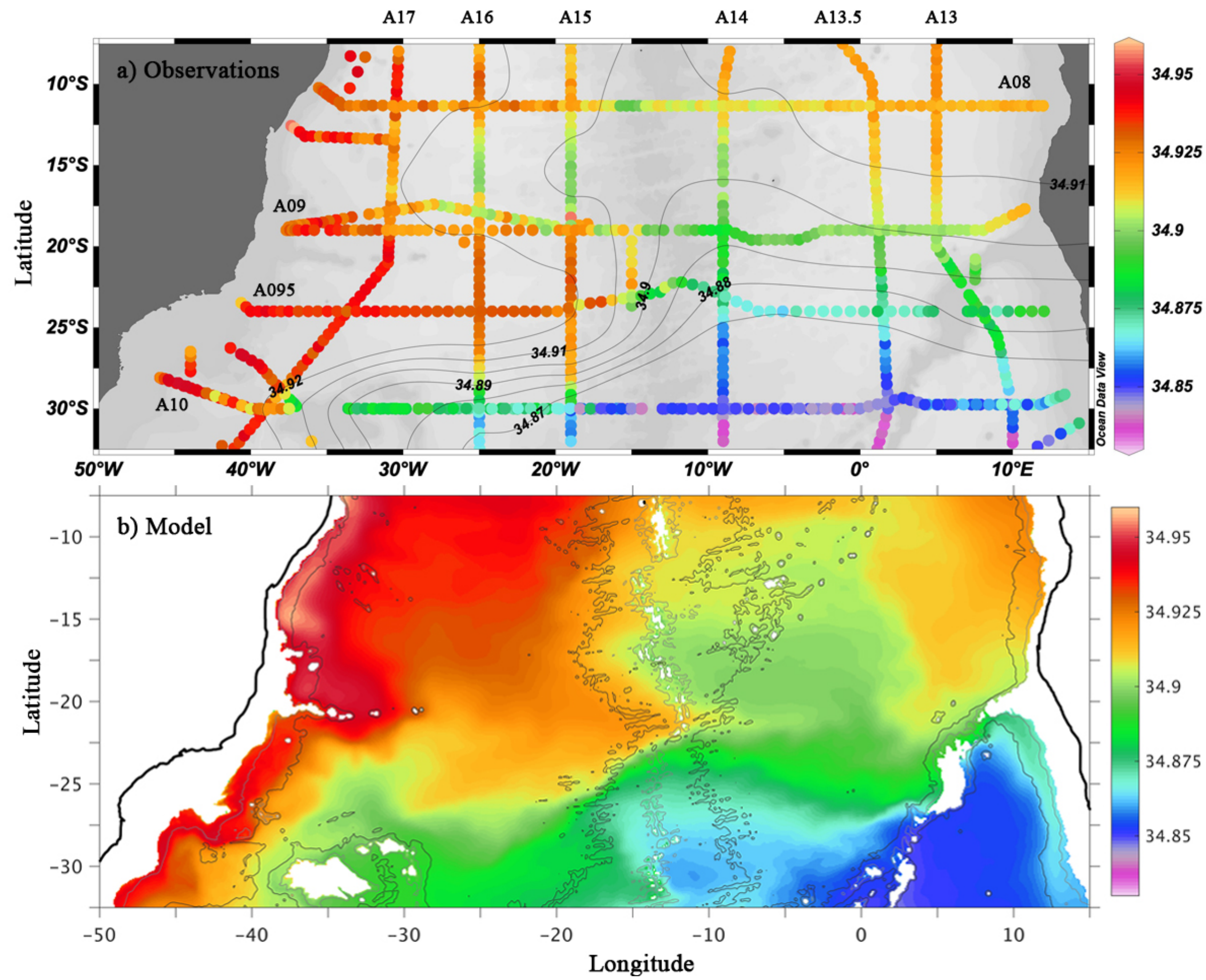

Figure 19: a) observed and model salinity distribution at 2500 m in the South Atlantic. Observation based on CTD data from GoShip program http://www.go-ship.org. Detailed vertical sections can be seen in the WOCE Atlas (Kiltermann et al., 2011). The results show an eastward extension of high salinity (NADW signature) between 20 and 25°S west of the mid-Atlantic Ridge (MAR), and significantly lower salinity east of MAR.

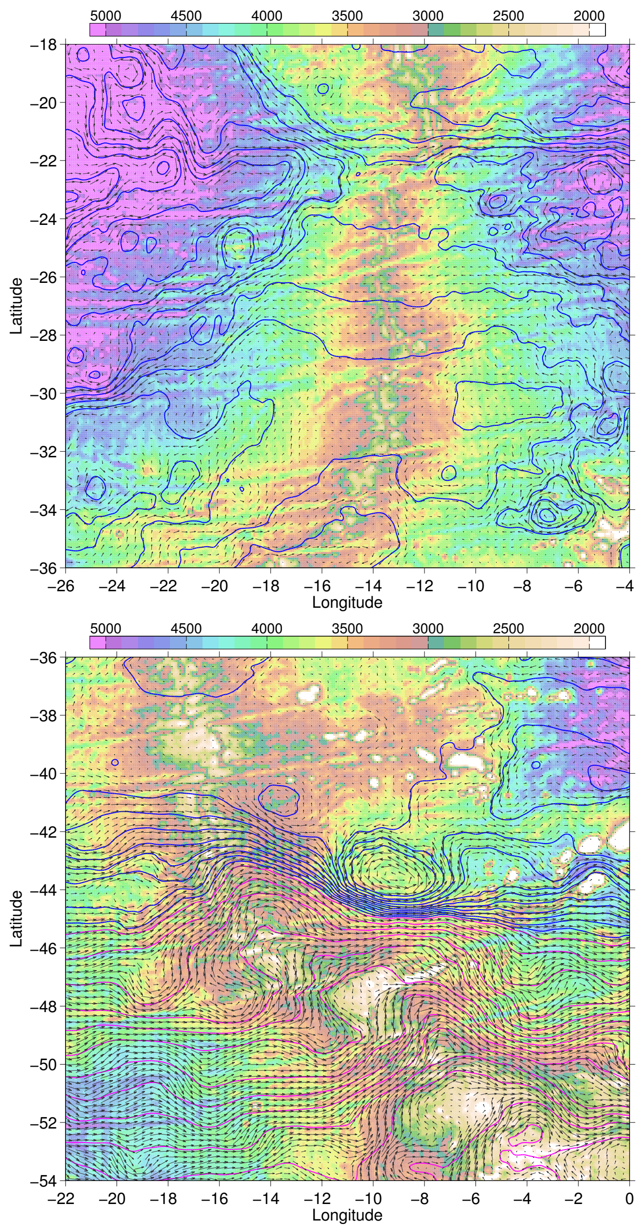

Figure 20: Zoomed view of the circulation for the density layer of NADW ($36.58 \leq \sigma_2 < 37.12\,\mathrm{kg\,m^{-3}}$) across the Mid-Atlantic Ridge in the South Atlantic Ocean. The blue contours denote NADW from north and magenta streamlines denote ACC from Drake Passage.

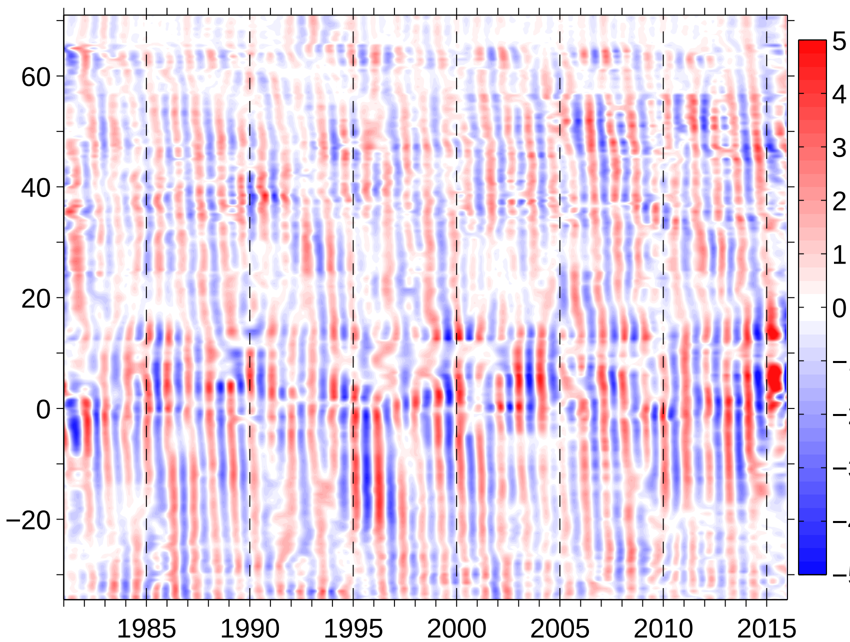

Figure 21: Modeled seasonal variability of the AMOC transports at different latitude, based on the third Intrinsic mode function (IMF) using the the ensemble empirical mode decomposition (EEMD, Huang and Wu (2008) and Wu and Huang (2009).

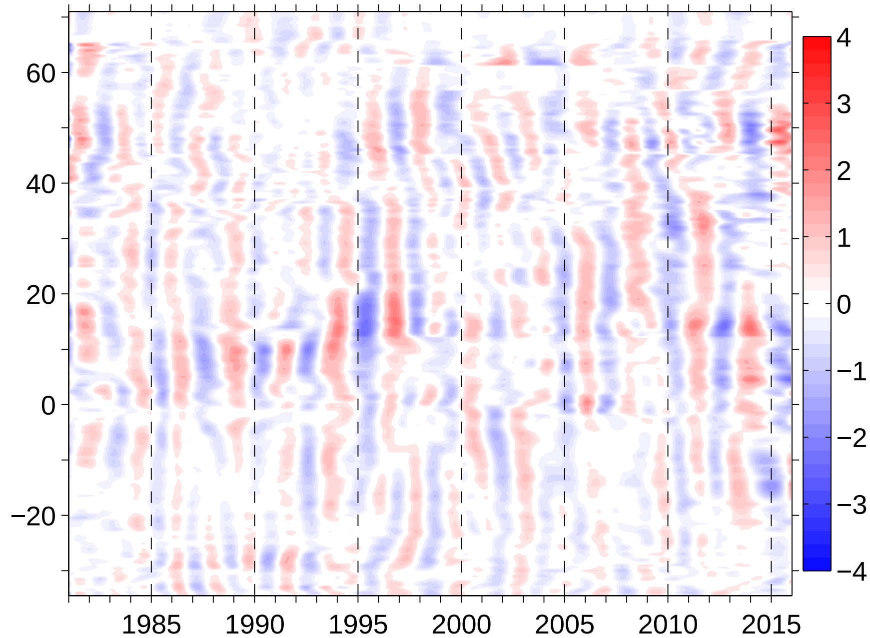

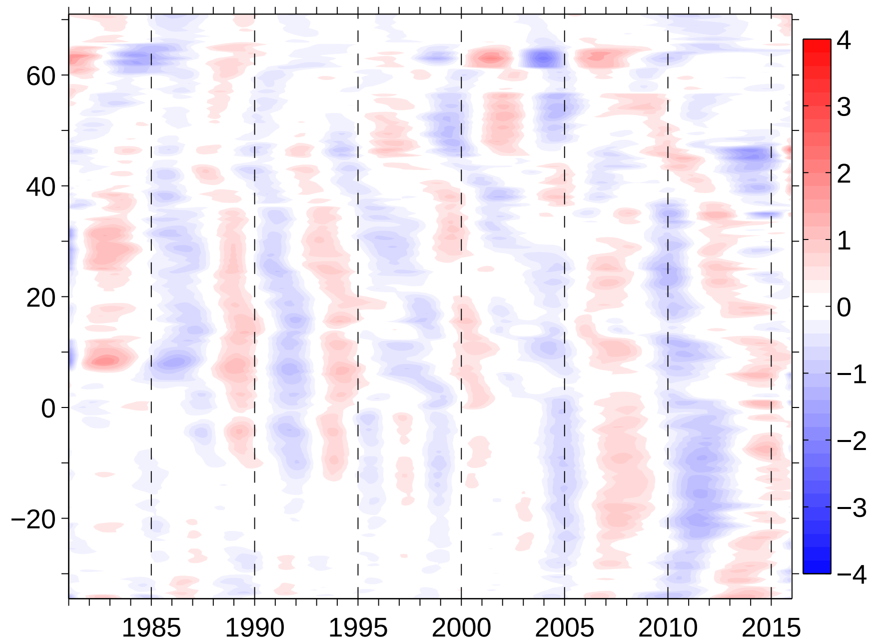

Figure 22: Modeled interannual variability of the AMOC transports at different latitude, based on the fourth and fifth Intrinsic mode function (IMF) using the ensemble empirical mode decomposition (EEMD, Huang and Wu (2008) and Wu and Huang (2009).

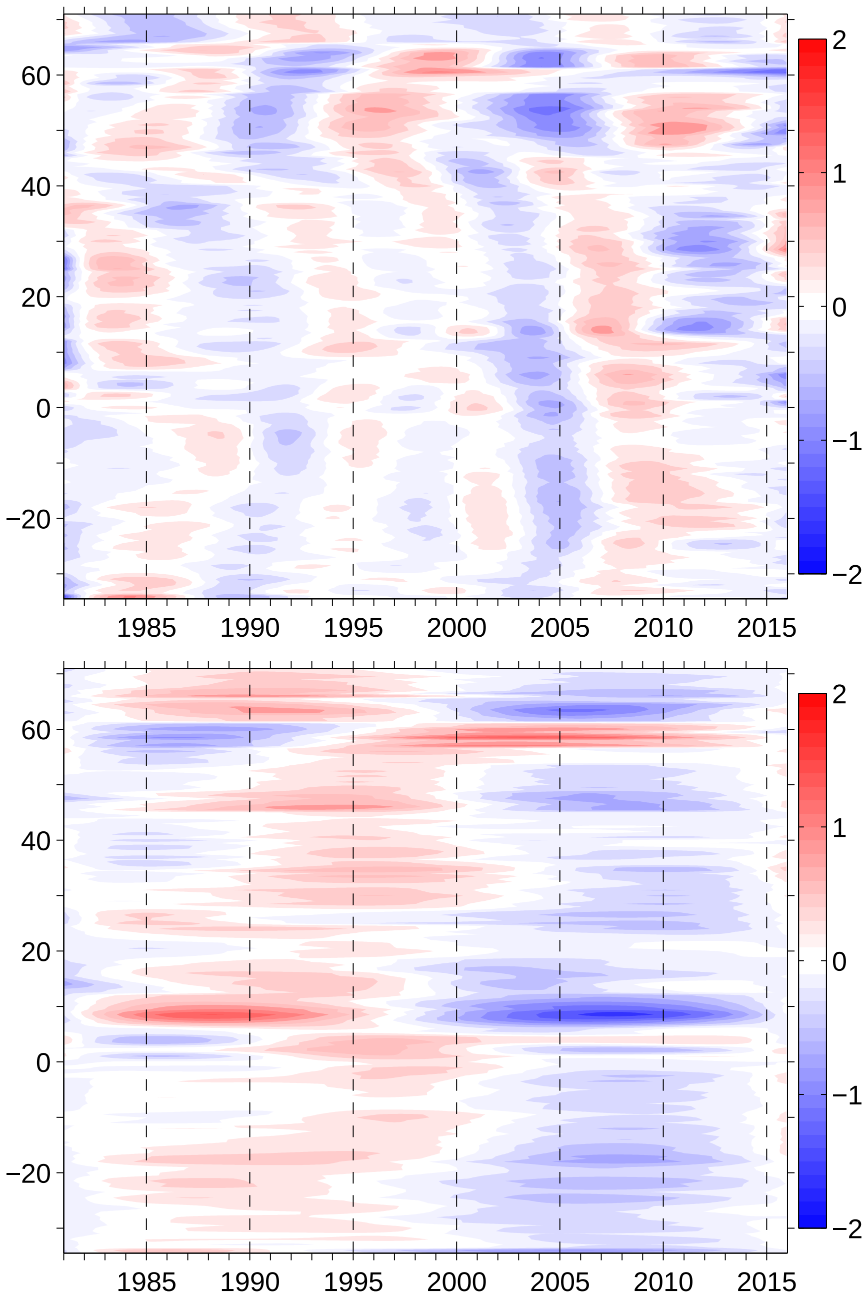

Figure 23: Modeled decadal variability of the AMOC transports at different latitude, based on the sixth and seventh Intrinsic mode function (IMF) using the ensemble empirical mode decomposition (EEMD, Huang and Wu (2008) and Wu and Huang (2009).